2017

Spatial Variability of the Depth to the Magma Reservoir Beneath the Yellowstone Caldera Inferred from Observations of Seiche Loading Induced Strain

Kevin James Gryger
Louisiana State University and Agricultural and Mechanical College

SPATIAL VARIABILITY OF THE DEPTH TO THE MAGMA RESERVOIR BENEATH THE YELLOWSTONE CALDERA INFERRED FROM OBSERVATIONS OF SEICHE LOADING INDUCED STRAIN

A Thesis

Submitted to the Graduate Faculty of the
Louisiana State University and
Agricultural and Mechanical College
in partial fulfillment of the
requirements for the degree of
Master of Science

in

The Department of Geology and Geophysics

by
Kevin J. Gryger
B.S., Stockton University, 2012
May 2017

ACKNOWLEDGMENTS

I thank my advisor Dr. Karen Luttrell of Louisiana State University for this research opportunity, for all of her help in planning for this project, revisions and editing of my thesis, and all of the long discussions about science. I thank my committee members Dr. Carol Wicks and Dr. Juan Lorenzo of Louisiana State University for their advice and inputs. I thank David Mencin of UNAVCO for his assistance in collecting absolute pressure gauge data in Yellowstone Lake, and for providing models of the shape of seiche waves in Yellowstone Lake. I thank Kathleen Hodgkinson of UNAVCO for assistance in the processing and calibration of borehole strainmeter data. I thank Madeline Myers and Louis Garcia of Louisiana State University for their work in deployment and recovery of data from absolute pressure gauges in Yellowstone Lake. I thank Pat Bigelow from the National Park Service for her time in taking us out on the boat in Yellowstone Lake to deploy absolute pressure gauges in back country locations.

TABLE OF CONTENTS

LIST OF TABLES

LIST OF FIGURES

ABSTRACT

Seiche waves in Yellowstone Lake at ~78, ~51, and ~25 minute periods and heights <10 cm can cause measurable strain (< 40 ns) as observed on borehole strainmeters both near (<300 m) and far (~20 km) from the lake. Observations of the correlation between the seiche waves and the associated strain response can be used to constrain the rigidity of the upper crust, the depth to magma bodies in the subsurface, and the viscosity (related to melt percentage) of the magma bodies in place. Lake level was directly measured with campaign absolute pressure gauges deployed in the West Thumb basin, Breeze Channel, and central basin of Yellowstone Lake, and 13 large seiche events (≥7 cm) were identified from these observations. Periodic strain transients were measured on borehole strainmeters in the caldera during the 13 large seiche events. The peak-to-trough amplitude and phase of the seiche wave and strain response were estimated by fitting a multi-frequency sinusoid to the time series over a 4-hour window during each seiche event. It was found that the relationship between an applied seiche load and the associated strain response is self-consistent and linearly proportional at each borehole strainmeter in the caldera. Over multiple seiche events the observed strain response is consistent with a modeled strain-field produced by a seiche load on a two-layered viscoelastic model defined by free parameters Young's modulus (E_1), plate thickness (H), and shear modulus ratio (μ_2/μ_1). The two-layered viscoelastic model represents a solid upper crust overlying a partially molten body which may be small pockets of melt (<1 km thickness) or a larger magma reservoir. Results suggest crystallizing melt beneath Yellowstone caldera at depths (H) of ~4–8 km in the south-southeast and ~3-5 km in the north-northwest sections of the caldera. Temporal observations between strain meters, coupled with constraints of Young's and shear moduli suggest that melt in the shallow crust has a viscosity $\leq 10^{13}$ Pa s.

CHAPTER 1. INTRODUCTION

The Yellowstone Plateau Volcanic Field is one of the largest active caldera forming volcanic systems in the world. In addition to its extensive hydrothermal network (i.e. geysers, hot springs, fumaroles), Yellowstone is also has significant heat flow, ground deformation, and seismicity centered on the 640 ka Yellowstone caldera [*Christiansen*, 2001]. This caldera is the result of the most recent in a series of large caldera forming eruptions that are a product of the hotspot that has made its impact from southeastern Oregon to northwestern Wyoming [*Smith and Braile*, 1994; *Smith and Siegel*, 2000]. The hotspot at its current location feeds into a magmatic system beneath the Yellowstone caldera. The continued characterization of the magma reservoir beneath the Yellowstone caldera is an important and ongoing concern for assessing hazard in the region [*Christiansen et al.*, 2007].

Two important factors in characterizing the hazard of a large volcanic system are the depth to the magma reservoir and the viscosity (related to melt percentage) of the magma in place [*Lowenstern et al.*, 2006]. Efforts to determine the structure of the magma reservoir have been conducted utilizing seismic tomography [*Chu et al.*, 2010; *Husen et al.*, 2004; *Miller and Smith*, 1999], ambient seismic activity [*Seats and Lawrence*, 2014], and gravity observations [*DeNosaquo et al.*, 2009] which suggest crystallizing magma in the crust as shallow as 3 km with a melt fraction between 8–50%. The spatial resolution for these methods may be several to tens of kilometers for seismic tomography and gravity observations, respectively. Therefore, these methods may miss small bodies (<1 km in thickness) of melt in the shallow crust such as sills or dikes, which themselves may have a larger percentage of melt than the larger magma body [*Lowenstern et al.*, 2006; *Vazquez et al.*, 2009].

Recent work in response to the discovery of anomalous periodic signals recorded on the network of borehole strainmeters throughout the caldera proposed a method to infer magma depth and its melt fraction [*Luttrell et al.*, 2013]. The study demonstrated that long period standing waves, seiche waves, within Yellowstone Lake of significant magnitude (>7 cm) acted as a load on the crust causing measurable strain observable on borehole strainmeters both near (<300 m) and distant (>20 km) from the lake. They suggested that the strain observed on the borehole strainmeters in the Yellowstone caldera is sensitive to bodies of partial melt in the subsurface. By modeling the strain signals, they constrained the shallow (<10 km) subsurface rheology within the Yellowstone caldera.

In this project we test the hypothesis proposed by *Luttrell et al.* [2013] that the seiche loading induced strain-field as observed on borehole strainmeters is sensitive to melt in the subsurface. The first step in testing this hypothesis is to collect additional data from more locations. Since August 2014, absolute pressure gauges have been deployed intermittently in the lake from West Thumb to the Southeast Arm to capture measurements of seiche waves from direct observations of lake level across Yellowstone Lake. In 2013 a decommissioned borehole strainmeter (B205), which lies on the northwestern rim of the caldera was replaced. The inclusion of this new borehole strainmeter (B950), provides an additional location to measure the induced strain-field that was not available during previous research. Second, we reconsider the analysis of *Luttrell et al.* [2013] and test new methods for synthesizing lake level and strain data and how the observations can be related to properties of the subsurface.

CHAPTER 2. LITERATURE REVIEW

2.1 The Yellowstone Plateau volcanic field

The Yellowstone Plateau volcanic field is one of the largest active large caldera forming volcanic systems in the world, and the largest in North America. Significant seismicity [*Farrell et al.*, 2010], ground deformation [*Chang et al.*, 2007], and hydrothermal activity [*Lowenstern and Hurwitz*, 2008] are centered on the youngest of the three recent calderas (<2.1 Ma) that formed during the 640 ka eruption [*Lowenstern et al.*, 2006]. Post-eruption, a series of rhyolitic lava flows filled in the large caldera (55 by 78 km), the most recent of which occurred 70 ka [*Christiansen et al.*, 2007]. These calderas are signatures of a mantle hotspot that underlies the Northwestern United States. The Eastern Snake River Plain traces the path of the North American plate over this hotspot [*Smith and Braile*, 1994]. On the southeastern edge of the caldera rests the large (350 km^2) freshwater Yellowstone Lake (Figure 2.1).

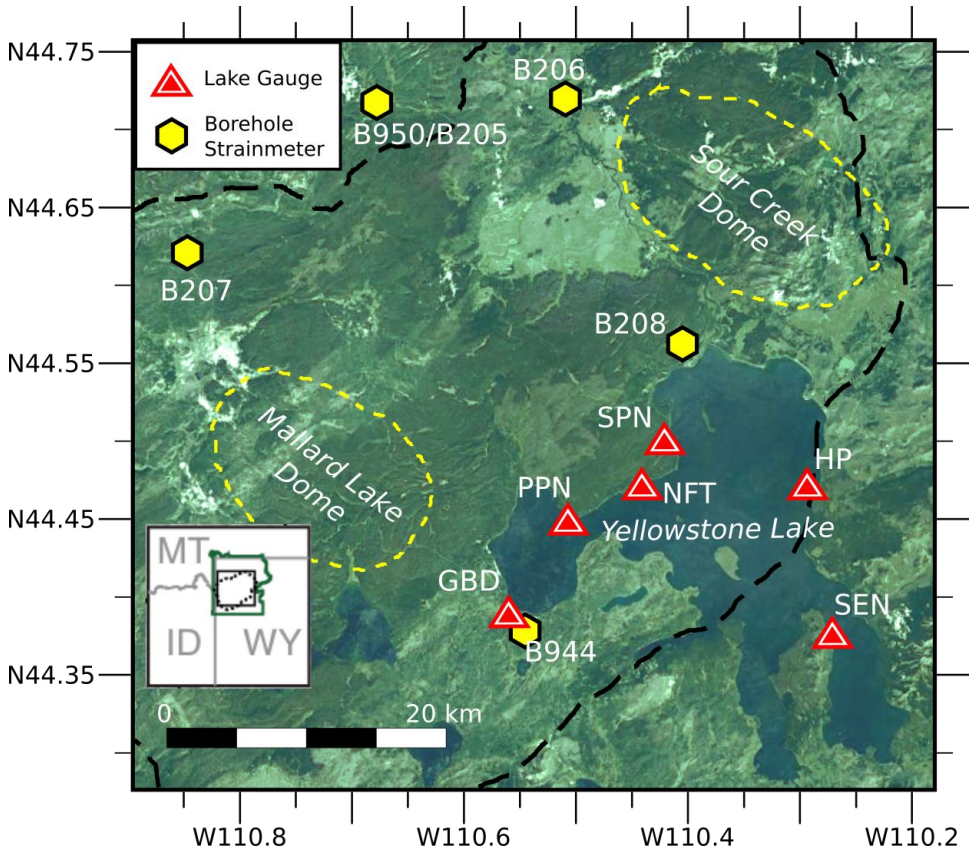

Figure 2.1: Map of the study region in Yellowstone National Park (green line in inset) with the estimated caldera boundary marked by the dashed black line, and regions of recent uplift marked by the dashed yellow lines at the resurgent domes. Borehole strainmeters (B206, B207, B208, B944, and B950/B205) and campaign absolute pressure gauges (GBD, PPN, SPN, NFT, HP, and SEN) are indicated by yellow hexagons and red triangles, respectively. Background imagery from Google Earth.

Extensive research in the region suggests that the Yellowstone volcanic field is still active and that a shallow magma body is present beneath the caldera. This is indicated by the extensive hydrothermal system, and geodetic surveys that demonstrated that the central region of the caldera had

risen 80 cm over a period of 50 years [*Pelton and Smith*, 1979]. The majority of this crustal deformation and uplift tends to be centered on the two resurgent domes, the Mallard Lake and Sour Creek domes. The rate of this ground deformation in the caldera has fluctuated over time with a recent increase and then subsequent decrease in ground uplift from 2004 to 2006 [*Chang et al.*, 2010]. These variations in uplift were attributed to large expanding intrusions at depths up to 10 km and redistributions of near surface hydrothermal fluids [*Chang et al.*, 2007]. Studies of the subsurface beneath the Yellowstone caldera utilizing seismic tomography suggest that the there is a low velocity body within the shallow crust greater than 1000 km^3, and some estimations suggesting 4,300 km^3 [*Chu et al.*, 2010]. The upper limits of this magma body have been placed as shallow as 3 km [*Chu et al.*, 2010], 6 km [*Miller and Smith*, 1999], and as deep as 8 km [*Husen et al.*, 2004]. The depth of local seismicity also has inferred the depth of the brittle-ductile transition zone at 4–6 km from the caldera surface [*Smith et al.*, 2009]. Analysis of the relative P and S wave velocities suggest the shallow magma body has melt fractions ranging from 32% [*Chu et al.*, 2010], 8-15% [*Smith et al.*, 2009], and 10-50% [*Lehman et al.*, 1982]. Monitoring of ambient seismic activity has shown the presence of a low velocity (~25% slower than the regional average) anomaly beneath the caldera surface, which was interpreted to be a crystalizing magma at depths of 5-8 km [*Seats and Lawrence*, 2014]. A low density body that varies spatially (2520 kg/m^3 in the caldera proper, 2470 kg/m^3 in the northeast section) has been interpreted as a body of melt at depths greater than 10 km [*DeNosaquo et al.*, 2009]. The composition of the magma bodies present beneath the caldera have been inferred from a combination of petrologic and geochemical methods [*Christiansen et al.*, 2007; *Hildreth*, 1981; *Hildreth et al.*, 1991]. This has led to the interpretation that there is a combination of rhyolitic magmas shallow in the crust with deeper basaltic magmas [*Christiansen et al.*, 2007; *Hildreth*, 1981; *Hildreth et al.*, 1991].

All of these methods and studies have contributed to the continued study of the Yellowstone Volcanic Field, which is important for the ongoing assessment of geological hazards for the region. However, a single method is incapable of fully characterizing the composition and structure of the magma system in place beneath the caldera. Every method is influenced differently by varying physical properties such as the percent melt, density, pressure, or the composition. In general, these methods are useful for determining the average bulk properties of the volume within the crust, but depending on varying spatial resolutions may have difficulty resolving smaller scale features that reside closer to the surface. For example, this spatial resolution may be several kilometers and go up to tens of kilometers for seismic tomography and gravity observations, respectively. Therefore, interpretations from seismic tomography and gravity observations may miss small bodies (<1 km in thickness) of melt in the shallow crust such as sills or dikes, which themselves may have a larger percentage of melt than the larger magma body [*Lowenstern et al.*, 2006; *Vazquez et al.*, 2009]. Seismic tomography relies on rays propagating through the deep crust using subtle timing differences to indicate features in the crust. For a small feature (e.g. sills or dikes) the timing difference may be too small to distinguish it from the larger timing differences generated from larger features such as the main magma reservoir. Typically gravity surveys have a low resolution because of the upward continuation of the actual gravity anomaly through the crust. Therefore, all the effects are integrated together and small scale features would become indistinguishable from the larger mass of the main reservoir.

Luttrell et al. [2013] proposed that the relationship between seiche waves in the Yellowstone Lake and the deformation they cause is most sensitive to shallow bodies of melt in the crust such as sills or dikes. This is because the seiche load does not have to propagate through the full upper crust to generate the observed strain on the far side of the caldera. The load from the lake is entirely accommodated within the shallow crust. Therefore, with observations of the load and the associated strain, we can infer properties of the shallow crust and potential small melt bodies within it.

2.2 Relationship between seiche loading and strain in the Yellowstone caldera

Luttrell et al. [2013], first demonstrated that sudden onset high-amplitude seiche waves in Yellowstone Lake were causing measurable deformation within the caldera both near (<100 m) and distant (>20 km across the caldera) from the shores of the lake. Investigation into this phenomenon began after July 2009. During a routine inspection of data from borehole strainmeter B944, network operators at UNAVCO discovered a high amplitude signal with a consistent period of ~78 minutes. This had a sudden onset, maintained a high amplitude for up to 12 hours, and then gradually decayed over a few days. This signal was simultaneously observed at additional borehole strainmeters within the caldera. The anomalous strain transient had nearly the same onset time as high amplitude seiche waves in Yellowstone Lake, and the long period of the strain signal matched both the long period of the seiche waves observed at the lake basin and the period of the theoretical fundamental seiche mode predicted for Yellowstone Lake. These seiche events with associated strain response occur year round, even when the lake is covered in ice. However, the strongest of these events tend to occur in the summer when there is no ice cover [*Luttrell et al.*, 2013].

This relationship between seiche waves in Yellowstone Lake and the associated strain response has several defining features that provide a unique set of observations that can be used in examining the subsurface beneath the Yellowstone caldera. The longest natural period of a seiche wave in a standing body of water is dependent of the shape of the basin, meaning that as long as there are no major changes to the basin itself, the period of the seiche will remain constant over time. This has been shown to hold true for the seiche waves in Yellowstone Lake with the ~78 minute period seiche varying less than 2 minutes as observed in available records of lake level. This seiche signal and its related strain response are distinguishable from other possible sources of noise and deformation (e.g., lower frequency tidal or diurnal signals, or higher frequency seismic or localized noise) because of their particular period. This seiche related deformation has been observed on borehole strainmeters both proximal (at B944 and B208) and distal (B207, B205, and B206) from the shores of the lake. These observations provide a spatially distributed sampling of the seiche-induced strain field. Finally, there has been no observed significant delay (≤25 minutes) in the onset time between a seiche wave measured in Yellowstone Lake, the strain response measured near the lake (B944), and strain response measured far from the lake (B206) [*Luttrell et al.*, 2013]. From these observations it was suggested that the crustal deformation occurs due to mechanical rebound in response to the varying water load on the earth's crust. This is in contrast to the mechanism of pore pressure diffusion, where expected delay in onset times would be hours to days [*Luttrell et al.*, 2013].

From their analysis and model evaluation, *Luttrell et al*. [2013] discovered that a two-layered viscoelastic half-space model was capable of producing crustal strains that are within the same magnitude as those observed on borehole strainmeters in the Yellowstone caldera. They were able to infer the upper limits of the magma reservoir to be 3–6 km beneath the caldera surface and the magma in place to have a melt viscosity less than 10^{11} Pa s (consistent with a mush of 35% melt fraction). These findings were consistent with seismic tomography, crustal deformation, and gravity observations that suggest there is molten magma at depths of 3-10 km with a melt fraction of 10-30% [*Chang et al.*, 2010; *Chu et al.*, 2010; *DeNosaquo et al.*, 2009; *Husen et al.*, 2004; *Seats and Lawrence*, 2014; *Wicks et al.*, 2006].

CHAPTER 3. DATA AND INSTRUMENTATION

3.1 Lake observations and seiche records

In an effort to improve the characterization of seiche waves occurring in Yellowstone Lake, absolute pressure gauges (APGs) were deployed intermittently from August 2014 - September 2016 at several different locations within the lake. The absolute pressure gauges measure the difference between pressure above the water and the pressure at depth which is related to the amount of water between the two. The instruments can record seasonal changes in the lake, periodic variations (i.e. seiche waves), and localized higher frequency perturbations (i.e. wind driven waves). In the West Thumb basin, instruments were deployed at Grant boat dock (GBD) and near Pumice Point (PPN) (Figure 2.1). In the central basin, pressure gauges were deployed near Sand Point (SPN) and Holmes Point (HP). In Breeze Channel, an instrument was deployed at the North Fir Turnout (NFT). Finally, the last instrument was deployed in the Southeast Arm (SEN). At this time, the GBD installation is the only (semi-) permanent campaign deployment. These deployment locations were chosen based on the model of the ~78 minute period wave (Figure 3.1) to capture measurements of the ~78 minute period seiche waves as they traveled across the lake basin [*Luttrell et al.*, 2013].

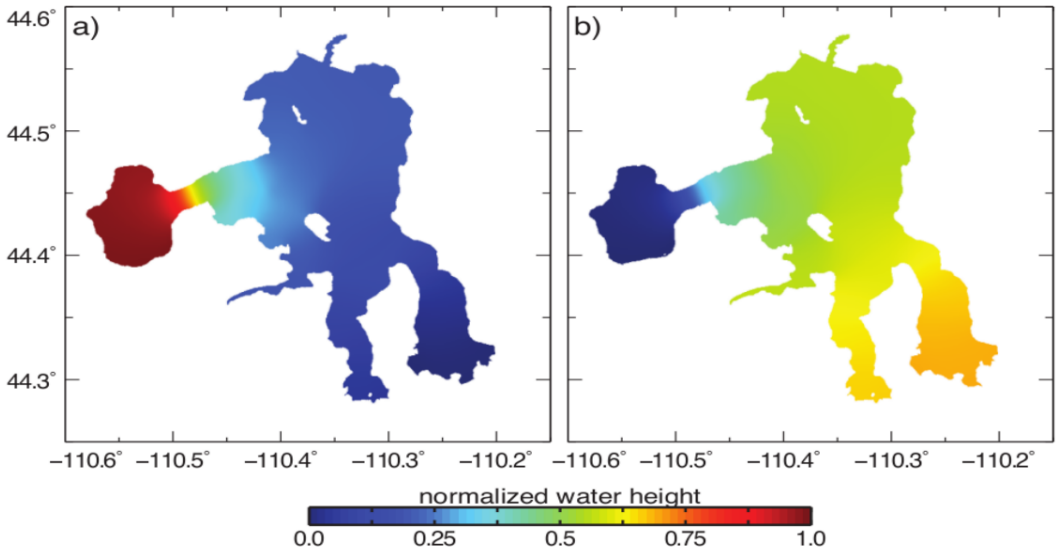

Figure 3.1**:** Modeled distribution of lake water during the (a) "peak" and (b) "trough" of the primary (~78 minute period) seiche mode in Yellowstone Lake. After *Luttrell et al.*, 2013.

From August 2014 to September 2016, 61 weeks of data was collected from the lake gauge at GBD (Figure 3.2). Combined with the data from the pilot study, this totals the data from GBD to 78 weeks from August 2011 to September 2016 [*Luttrell et al.*, 2013]. At PPN and SPN, 36 weeks of data were collected. In September 2015, the instruments at SPN and PPN were recovered and then refurbished. Those instruments were redeployed at HP and SEN in June 2016. Four weeks of data at the central basin were collected at HP. The APG from HP was then moved to a new location at NFT. Ten weeks of data have been collected from the breeze channel at NFT. At the time of writing, no data has

been recovered from the APG deployed at SEN. For this project we consider observations at GBD, SPN, and PPN. For complete list of collected lake data see Table A.4.

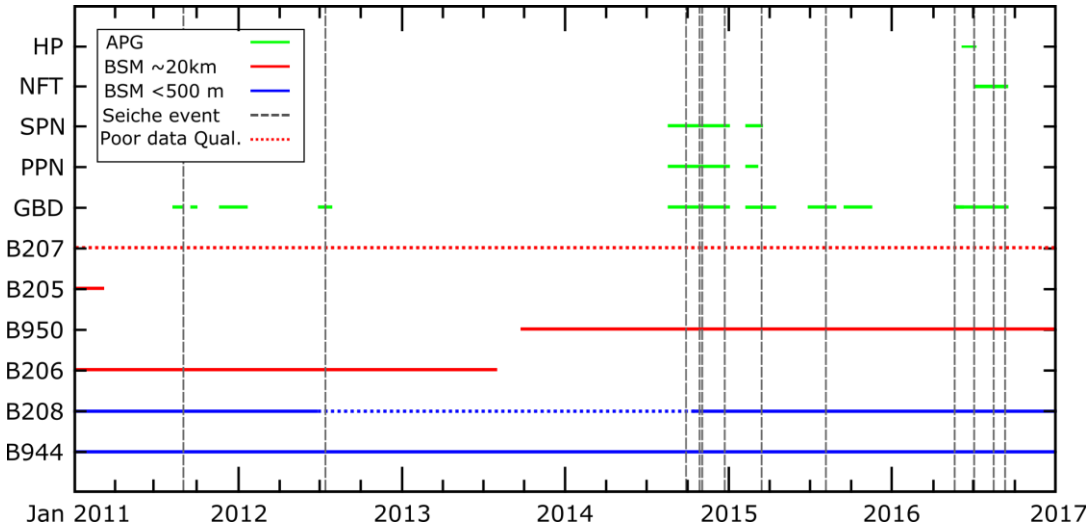

Figure 3.2: Timeline of when data is available on borehole strainmeters near (blue) and distant (red) from Yellowstone Lake. Times of collected absolute pressure gauge data are indicated in green. Vertical grey dashed lines indicate measured large amplitude seiche wave (>7cm). Although B207 and B208 have been active since their installation in 2008, data has not consistently been viable for use (dotted sections). For list of collected lake data see Table A.4. List of large seiche events Table A.6.

3.2 Borehole strainmeter data acquisition

Five Plate Boundary Observatory (PBO) borehole strainmeters are installed in Yellowstone National Park. Borehole strainmeters are highly sensitive instruments that can resolve deformations less than nanostrain (a micron in length of change over a kilometer). These borehole strainmeters were installed to expand the PBO geodetic network and capture transient strains that are between the sampling envelopes captured by GPS receivers and broadband seismometers [*Hodgkinson et al.*, 2013]. Two of the boreholes strainmeters (B944 and B208) are installed close to the shore of Yellowstone Lake (<100 m), which lies over the southeastern edge of the Yellowstone Caldera (Figure 2.1). The remaining three borehole strainmeters (B205, B207, and B206) are located along the northern and north-western boundaries of the Yellowstone Caldera (Figure 2.1). Borehole strainmeter B205 was decommissioned due to failure in 2011 and later replaced with B950 (Figure 3.2). Borehole strainmeter data was retrieved from the Incorporated Research Institutions for Seismology (IRIS) databases for the time periods where there is recovered lake data.

The ability to characterize a seiche wave and its associated deformation is limited by the number of instruments recording viable data simultaneously. Of the five borehole strainmeters installed in Yellowstone, no more than three are ever fully operational during a time when there are lake measurements (Figure 3.2). Only B944 has been operational and records usable data since its installation. Although operational since its installation, B207 does not record viable data and will not be utilized for this project. B208 intermittently records data that is suitable for the purposes of this research. *Luttrell et al.* [2013] based their results on observations from B206. As of 2013 the signal quality of data from B206 had degraded beyond usability. B950 was installed in 2013 and has remained operational. Ideally,

there are absolute pressure gauges in the lake at multiple locations with operational borehole strainmeters both near and far from the lake recording data simultaneously. From our collected data this occurs between September 2014 to March 2015 where there is lake data from three locations (GBD, SPN, and PPN) and operational borehole strainmeters near (B944 and B208) and far (B950) from the lake. It is more typical for there to be one pressure gauge measuring data in the lake, two operational borehole strainmeters near the lake, and one operational across the caldera. The ability to analyze seiche induced strain, and relate it to the subsurface decreases significantly with a decrease in the number of operational strainmeters far from the lake (B950 and B206). This is because the strain-field observed at the distant borehole strainmeters is more dependent on the structural and rheological properties of the caldera between them and the lake than the strain-field observed near the lake.

3.3 Processing and calibration of borehole strainmeter data

The borehole strainmeters in Yellowstone are Gladwin Tensor Strainmeters, which consist of four extensometers (referred to as gauges) that measure the changes in the diameter of the strainmeter housing at different azimuths [*Hodgkinson et al.*, 2013; *Roeloffs*, 2010]. Before observations from borehole strainmeters can be utilized in geophysical models, it is necessary to "calibrate" the output. The process of calibration takes the individual gauge elongation measurements and transforms them into measurements of horizontal 3-component formation strain, areal (ε_A), differential (ε_D) and engineering shear (ε_S) strain. We calibrate B206 and B944 using calibrations matrixes determined by *Hodgkinson et al.* [2013] (Table A.3) where the calibration matrix is applied to the data to convert from gauge elongations to formation strain. For borehole strainmeters B208 and B950 calibration matrixes were generated using the methods of *Hodgkinson et al.* [2013]. Calibration matrixes can be computed by comparing the real and imaginary components of the M_2 and O_1 earth tides recorded by each gauge (Table A.1) with the corresponding components of the tides as predicted by tidal models (Appendix A.2) [*Hodgkinson et al.*, 2013]. To account for uncertainties in the calibration process we consider an error of ±25% for an observed strain value.

We further process borehole strainmeter data by removing instrumental artifacts, such as hourly calibration pulses, and gaps and outliers in the data. Additionally, borehole strainmeters show a coseismic step response to creep events in active fault systems [*Roeloffs*, 2010]. The instrumental artifacts and coseismic step responses interfere with Fourier analysis. We correct for the steps by removing them from the time series, then readjusting to start at similar values.

Earth tides measured on the borehole strainmeters are readily identifiable and the amplitude and phase of various earth tides have been estimated from individual gauge elongations (Table A.1) [*Hodgkinson et al.*, 2013; *Roeloffs*, 2010]. While these tides occur at much longer periods than the sub-diurnal seiche signals, they can still interfere with analysis and synthesis of the data. To minimize the effect of the Earth tides we remove the M_2 and O_1 earth tides by subtracting a modeled earth tide signal constructed with the estimated tidal components (Table A.1) from the gauge elongation data prior to calibration.

3.4 Atmospheric coupling of borehole strainmeters

It has been well documented that the strain measured PBO borehole strainmeters are coupled to vertical strain produced at the Earth's surface or a source within the Earth (subsurface fault slip or magmatic upwelling), which can be related to the areal strain. The strainmeters response to atmospheric pressure contains information about the vertical coupling [*Hodgkinson et al.*, 2013; *Roeloffs*, 2010]. Changes in atmospheric pressure impose a vertical stress that leads to both vertical and horizontal strains in the subsurface.

In this project we experimented with removing the strainmeter response to atmospheric pressure changes by using methods from *Hodgkinson et al.* [2013]. The barometric response coefficients for each gauge of a strainmeter from *Hodgkinson et al.* [2013] represent the change in measured nanostrain per change in barometric pressure. The strainmeters response to atmospheric pressure can be effectively removed by multiplying a time series of the local relative atmospheric pressure change by the barometric response coefficients and then subtracting the resultant time series from the corresponding gauge elongations. A barometric pressure gauge is co-located with each borehole strain meter recording at both 30-minute and 1-second sample rates. However, not all of the barometric pressure gauges are recording viable data. The 30-minute sampled pressure data is just about half the period of the dominant seiche related strain in the Yellowstone caldera (~78 minutes) and may not correct at a fine enough resolution for our analysis. Therefore, we focused on experimenting with available 1-second sampled data (measured at B208), decimated to ten second intervals. We decided on using the 1-second barometric pressure from B208 because it was the most consistent and free of gaps, spikes, and offsets. By comparing corrected, uncorrected, and data of the relative atmospheric pressure change we found that the available barometric response coefficients did not sufficiently remove the strainmeters response to pressure changes, particularly at B950. In some cases there was overcorrection of the strain data, where the "corrected" time series followed the atmospheric pressure data even more than the "uncorrected" time series. We also found that if a peak rapid change in atmospheric pressure was out of phase with the associated strainmeter response (e.g., due to the distance between the locations of atmospheric pressure and strain measurements), the correction would be at the wrong time and artificially introduce an even larger spike. Therefore, from our experiments we decided to proceed with analysis of the strainmeter data without using the available coefficients to correct for atmospheric pressure. We expect that the presence of atmospheric pressure-related signals in the strain time series does not interfere with the specific period range we consider (i.e., ~15–90 minutes). The implications of this assumption for our analysis are discussed further in section 4.5.

CHAPTER 4. SEICHING AND STRAIN RESPONSE

4.1 Seiche wave observations and spectral content

The filtered lake gauge data at GBD was examined in the time domain to identify significantly large seiche events. Seiches are identified in time and frequency domains by their characteristic period. The longest natural period of a seiche wave is dependent on the shape of the basin it is in. This period will remain relatively constant throughout time unless there is a significant change to the basin bathymetry. Previous work has established that the most dominant seiche modes in Yellowstone Lake correspond to periods of ~78 minutes, ~51 minutes, and ~25 minutes [*Luttrell et al.*, 2013]. A catalog the seiche events, including onset time, end time, the absolute maximum peak-to-trough amplitude, and the time of maximum amplitude is given in Table A.5. This process was repeated for the lake data collected at SPN and PPN, using the onset times of seiche events measured at GBD as a reference.

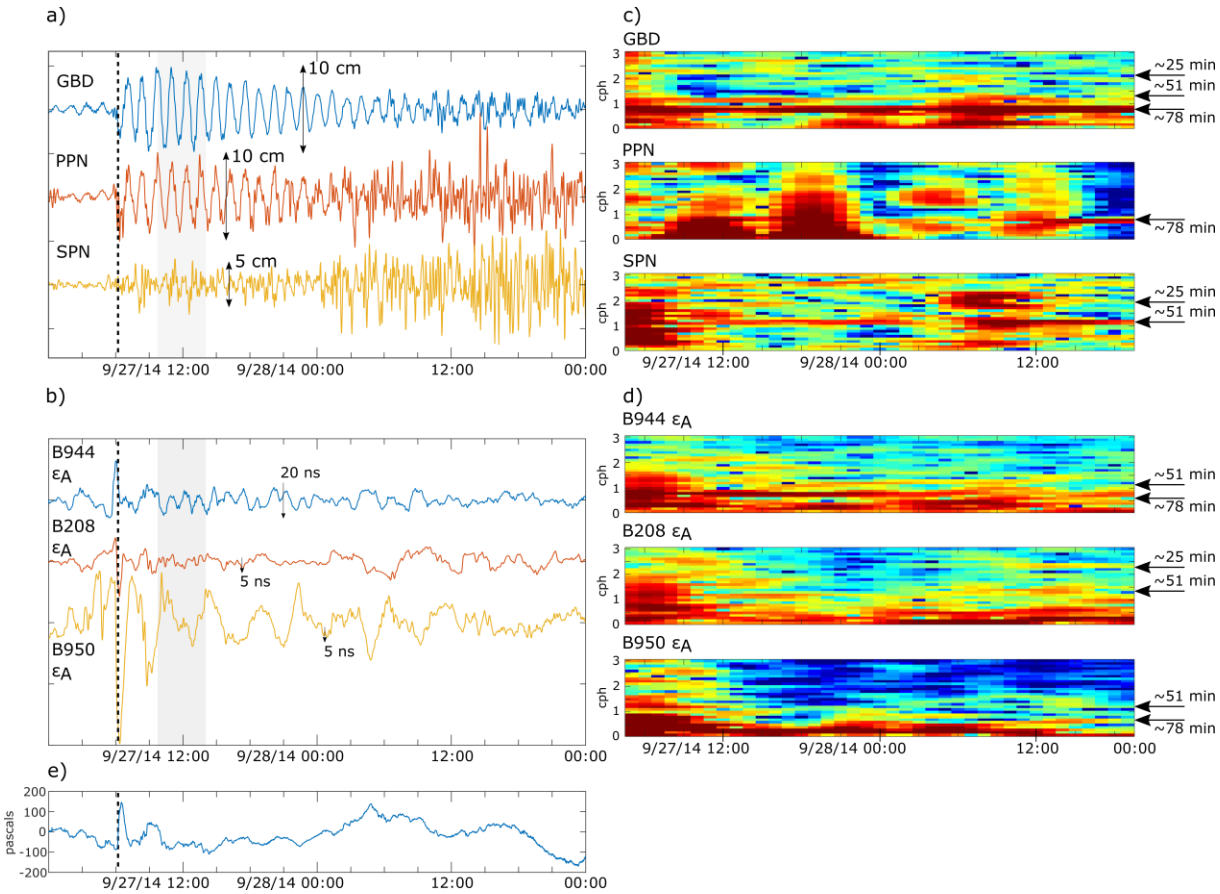

Figure 4.1**:** Prominent sudden-onset large-amplitude seiche and associated ε_A component beginning on 27 September, 2014, as recorded on (a) absolute pressure gauges and (b) borehole strainmeters. Grey bar indicates 4-hour measurement window from which the measured range was determined. Dashed black line indicated onset of seiche event and associated deformation concurrent with relative sharp increase in atmospheric pressure. Spectrograms of seiche event as observed on (c) absolute pressure gauges and (d) borehole strainmeters highlight the dominant modes of seiching in the lake and on borehole strainmeters (indicated by black). Vertical axis is in cycles per hour (cph). Warmer colors indicate greater spectral density. (e) Relative atmospheric pressure change in as recorded at B208.

From the 78 weeks of lake data collected at GBD, 70 seiche events were measured (Table A.5). One of the largest of these events occurred on 27 September 2014 (Figure 4.1a). In general, we found that the maximum peak-to-trough amplitude of a single seiche wave is greatest at GBD (Figure 4.1a, blue) and decreases going across the lake (PPN, Figure 4.1a, red) into the central basin as measured at SPN (Figure 4.1a, orange). Additionally, we find that the onset time of a seiche event to be consistently concurrent with a rapid change in atmospheric pressure (Figure 4.1a and 4.1e).

Spectral density analysis of the collected lake gauge data was used to identify the dominate periods (modes) of seiche waves in Yellowstone Lake. Three main signals are observed that oscillate at ~0.8, ~1.2, and ~2.5 cycles per hour (cph). That correspond to seiche waves with ~78, ~51, and ~25 minute periods (Figure 4.1c). In West Thumb basin the ~78 minute period seiche has a stronger presence while the ~51 and ~25 minute period seiches are either muted or not present as observed at GBD (Figure 4.1c, top) and PPN (Figure4.1c, middle). In the central basin at SPN it was observed that the ~51 minute period seiche is dominant with a muted presence of the ~78 and ~25 minute period seiche waves (Figure 4.1c, bottom). These results suggest that the dominate period of seiching in Yellowstone Lake changes spatially. Additionally, the presence of a strong ~78 minute period seiche component at PPN is inconsistent with the model of the seiche wave (Figure 3.1) that suggests PPN is a nodal point of the wave.

There is significantly more localized higher frequency noise measured at PPN and SPN compared to GBD that can be observed in both time (Figure 4.1a) and frequency domains (Figure 4.1c). This level of higher frequency noise tends to increase several hours after onset of a seiche. This difference in the higher frequency components of the data could be attributed to the location of the instruments. The pressure gauge at GBD is in a protected marina, so the effects of wind waves formed on the open lake basin (as seen at SPN and PPN) are minimized.

4.2 Strain response observations and spectral content

After the calibration of borehole strainmeter data we processed the data to minimize the presence of non-seiche related signals. The data was de-trended by computing the least square fit of a straight line to the data and removing the resulting function from the data. The time series data was run through a band-pass filter between 15 minutes and 8 hours to remove any remaining unwanted low frequency signals and higher frequency wave motion due to wind. These cutoffs were determined to be the optimal band that would sufficiently filter the data while not adversely affect the desired signals (Appendix A.2).

We examined the filtered and detrended areal, differential, and engineering shear strain data at each borehole strainmeter in time and frequency domains during times when there is significantly large seiching in the lake. We define a seiche event as significantly "large" if it has a maximum peak-to-trough amplitude $\geq$7cm. This size of seiche wave was chosen because only seiche waves of this size consistently produce measurable strain at distances >20 km from Yellowstone Lake, as observed at B950 and B206. Of the 70 seiche events recorded at GBD (Table A.5), 13 have a peak-to-trough amplitude $\geq$7 cm (Figure 3.2). These 13 events include the large seiche event used by *Luttrell et al.* [2013] that occurred on 12 July 2012. Of these measured events, only 5 were recorded at PPN and SPN. Due to changes in strainmeter performance over time, not all strainmeters record signals associated with each large seiche. B944 shows a strain response during all 13 of the seiche events. B950 has only been operational long enough to record a strain response during 11 of the seiche events. B208 has had usable data for the last 11 seiche events. Finally, only during two seiche is there an observable strain response at B206.

Spectral density analysis of strain measured at each strainmeter was used to determine the periods of strain transients present and if the periods were comparable to the identified seiche waves. At B944 during all 13 large seiche events we observed strong periodicity at ~78 minutes, with a muted signal with a ~51 minute period (Figure 4.1d, top). Spectrograms during the large seiche events measured at B208 show strong periodicity at ~51 minutes with muted sometimes nonexistent signals at ~78 and ~25 minute

periods (Figure 4.1d, middle). At B950 (Figure 4.1d, bottom) and B206 we observed strong periodicity at ~78 minutes, with muted signals with a ~51 and ~25 minute period. The ~25 minute period signal could also be absent from the B950 and B206 data. These periodic strain transients correlate to the ~78, ~51, and ~25 minute period seiche waves observed on the absolute pressure gauges in Yellowstone Lake. From these results we can see that the dominant period of strain response, and therefore the effect of a particular seiche wave, can vary spatially. This relationship is most apparent between B944 and B208. At B944 the strain response correlates strongly to the ~78 minute period seiche as measured in the West Thumb basin (GBD and PPN). Conversely, at B208 the strain response correlates more to the ~51 minute period seiche wave as measured in the central basin (SPN).

Much like seiching in the lake, the onset of the strain response is concurrent with a rapid change in atmospheric pressure (Figure 4.1a, c, and e). However, there are large fluctuations in the strainmeter measurements that correlate to rapid atmospheric pressure change. These fluctuations make determining the absolute onset time of a strain event in borehole strainmeter data challenging. After atmospheric interference subsides the seiche related strain is readily apparent in time and frequency domains occurring at ~78, ~51 minute, and ~25 minute periods. The strain persists at observable amplitudes up to 12 hours after onset at B944. The attenuation of the seiche related strain is faster at B950, B206, and B208 when compared to observations at B944.

For events that were measured at more than one strainmeter we directly compared the measured strain to make first-order qualitative observations of the behavior of seiche loading related strain. Consistently, B944 recorded well defined seiche related strain responses for all three strain components. B208 and B206 had the second highest signal quality. B950 consistently recorded seiche related strain with the least clarity. In general, we found that for any given load size, the strain response (ε_A, ε_D, and ε_S) measured at B944 (Figure 4.1b, blue) was significantly greater than the strain measured at B208 (Figure 4.1b, red), B950 (Figure 4.1b, orange), and B206.

4.3 Methods of sinusoid fitting

To quantify the amplitude of the identified seiche waves and the associated strain response we perform a least squares regression of sines and cosines to the time series data over a ~4 hour measurement window at periods of ~78, ~51, and ~25 minutes. The measurement window length was selected on the basis that over a period of ~4 hours the seiche related signals remained the most consistent (i.e. minimal attenuation). This window is placed after the maximum peak-to-trough amplitude of the seiche wave (i.e. after maximum loading), but during a time when there was minimal atmospheric interference in the strain data for each borehole strainmeter. Analysis by fitting sines and cosines to borehole strainmeter data has been successful in estimating the amplitude and phase of the M_2 and O_1 earth tides [*Roeloffs*, 2010]. The time series over the window $f(t)$, can be expressed as a sum of the component frequencies in two ways:

$$f(t) = \sum_{i=1}^{n} A_i cos(\omega_i t) + B_i sin(\omega_i t) \quad (1)$$

$$f(t) = \sum_{i=1}^{n} C_i cos(\omega_i t - \theta_i) \quad (2)$$

where for a single component (n) $C_n = \sqrt{A_n^2 + B_n^2}$ is the amplitude and $\theta_n = arctan(B_n/A_n)$ is its phase (in radians). We use the peak-to-trough amplitude ($2C_n$) for observations of seiche related activity and evaluation of geophysical models. Using equation (1) we estimated the peak-to-trough amplitude and relative phase for each seiche wave as measured on lake gauges and its associated strain response measured on the borehole strainmeters for each seiche event at ~78, ~51, and ~25 minute periods. Equation (2) facilitates the interpretation of the phase difference between a seiche wave measured in

Yellowstone Lake and the strain response measured near and far from the lake for a single seiche event. The effectiveness of the fit will be determined through a root mean squared error (RMSE):

$$RMSE = \sqrt{\frac{\sum_{t=1}^{n}(\hat{y}_t - y_t)^2}{n}} \quad (3)$$

where $\hat{y}_t$ is the modeled time series and y_t is the measured series. We also directly compare the modeled time series to the filtered data to assess the degree of fit. We use the relative change in lake level during a seiche event to quantify the loading effect the seiche has on the Earth's crust.

This method provides a consistent way to quantify the signals that are related to lake wide seiching. This is because we are able to identify the seiche related signals in both lake and strain measurements (via spectral analysis) then input the identified periods to the sinusoid fitting to isolated the desired signals. However, we must consider some of the limits of this method. Significant attenuation of the desired signal(s) can occur, even within the span of a measurement window (~4 hours). Even though we conducted these estimations on filtered borehole strainmeter data there is still a degree of noise (i.e. non seiche related strain). Therefore, this noise could increase the error between the fit and filtered time series curves. We must also ask if a ~4 hour measurement window is sufficient enough to quantify seiche related activity at the identified periods.

4.4 Amplitude and phase estimations of seiche waves and strain response

We fit a sinusoid to the lake and strainmeter data with a modeled signal of three frequency components that reflect the primary periods (~78 minute, ~51 minute, and ~25 minute) of seiche related activity as observed on the absolute pressure gauge in Yellowstone Lake and on the borehole strainmeters in the caldera. Figure 4.2 and Table 4.1 show an example of this fit for the seiche event that occurred on 27 September 2014. From the fitted sinusoid we determine the peak-to-trough amplitude for each component period (~78, ~51, ~25 minutes) of seiche waves as measured on absolute pressure gauges in Yellowstone Lake, and for each strain component (ε_A, ε_D, and ε_S) as measured on each of the borehole strainmeters in the caldera (Table 4.1). The fit is strongest in the lake pressure gauge data (Figure 4.2a). At B944 (Figure 4.2b) and B208 (Figure 4.2c) the fitting of the composite sinusoid is adequate, with an RMSE of <=25% of the maximum amplitude. As the amplitude of the seiche related signals becomes smaller and less defined the confidence of the fit decreases as seen at B950 (Figure 4.2d).

The RMSE for the composite signal is used to determine how well the least squares regression fits to the filtered data. Additionally the RMSE between the fit time series of an individual component period and the filtered lake or strain data can be used to show the relative presence of that component period. In some cases at B950 for individual frequency components (i.e. ~78, ~51, and ~25 minute period components), the calculated RMSE was larger than the peak-to-trough amplitude measurement itself. However, the RMSE between the composite sinusoid and the filtered time series remains less than the estimated amplitude for any one seiche event. This could mean that RMSE may not be the best method to approximate the degree of fit. Additionally, the large RMSE values for individual frequency components could arise because the signals we are trying to fit (i.e. ~78, ~51, and ~25 minute period components) are relatively small compared to non-periodic signals.

For the ~78 minute period component the estimated amplitude of the seiche waves in the lake range between 3.6-8.3 cm at GBD (for 13 events, Table A.6), 1.39-3.33 cm at PPN (for 5 events, Table A.6), and 0.0-0.3 cm at SPN (for 5 events, Table A.6). For the 13 events observed at B944, the estimated amplitude of areal strain ranges from 5-18 ns, differential strain from 4-18 ns, and engineering shear strain from 13-43ns (Table A.7). For the 11 events observed at B208, the estimated amplitude of areal strain ranges from 0.2-4 ns, differential strain from 0.1-1 ns, and engineering shear strain from 0.5-2.1ns (Table A.7). For the 11 events observed at B950, the estimated amplitude of areal strain ranges from 3-

12 ns, differential strain from 0.1-0.7 ns, and engineering shear strain from 0.1-1.2 ns (Table A.7). For the 2 events observed at B206, the estimated amplitude of areal strain ranges from 1.2-3.7 ns, differential strain from 0.5-1.1 ns, and engineering shear strain from 1.2-2.2 ns (Table A.7).

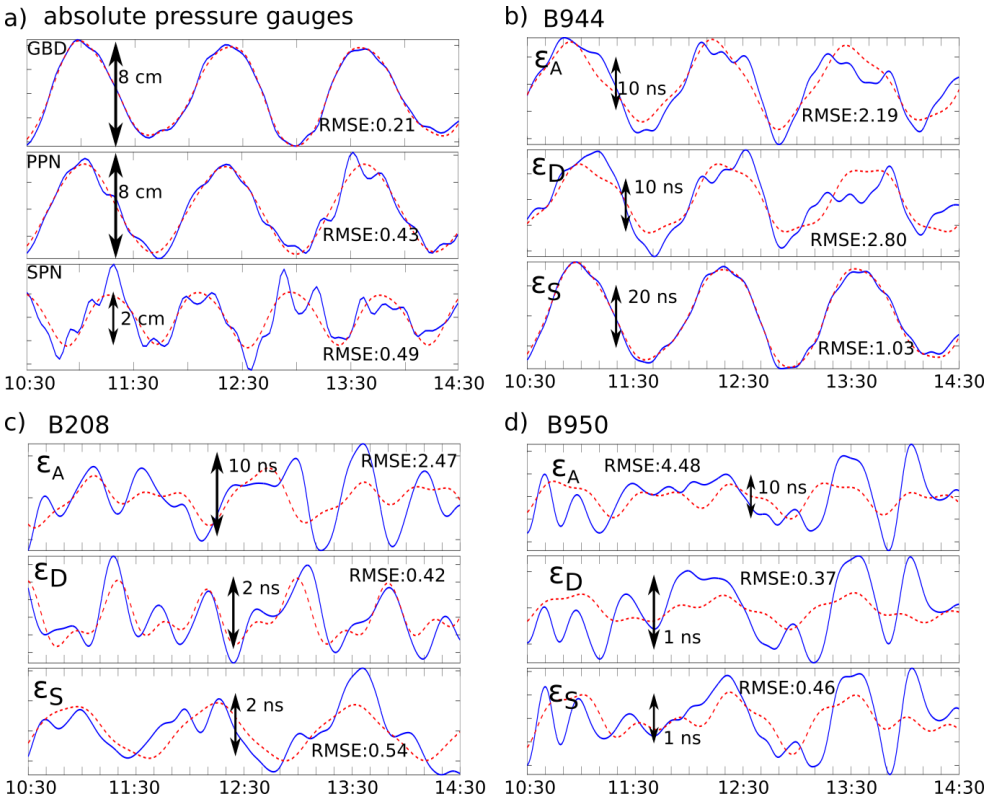

Figure 4.2: Seiche event from 27 September 2014 during ~4-hour measurement window (grey bar in Figure 4.2a and 4.2b) comparing filtered data (blue) and least squares regression curve (dashed red). The root mean squared error (RMSE) between the two curves is indicated. Data sets from lake pressure gauges (a) from GBD (top), PPN (middle), and SPN (bottom) are shown. Areal (ε_A, top), differential (ε_D, middle), and engineering shear (ε_S, bottom) strain components are shown from borehole strainmeters B944 (b), B208 (c), and B950 (d). Note that the vertical scales vary per plot. For amplitude and RMSE of each period component, see Table 4.1

We examined the estimated areal (Figure 4.3, top row), differential (Figure 4.3, middle row), and differential engineering (Figure 4.3, bottom row) strains at each of the strainmeters compared with the associated seiche wave amplitude. In general the results suggest a linear relationship between seiche load size and strain response for each strain component at borehole strainmeters B944 (Figure 4.3a), B208 (Figure 4.3b), B950 (Figure 4.3c), and B206 (Figure 4.3d). This means with increasing size of seiche waves in Yellowstone Lake, there is a proportional increase in strain within the caldera both near and far from the lake.

We compare the estimated strain responses between strainmeters using B944 as a primary reference point because the ~78 minute component is dominant and its proximity to GBD. For areal strain, observations at B944 and B950 (Figure 4.3a and c, top) differ by a factor of ~1.5-2, observations at B944 and B208 (Figure 4.3a and b, top) differ by a factor of ~5, and observations at B944 and B206 (Figure4.3a and d, top) differ by a factor of ~4. For differential strain, observations at B944 and B950

(Figure 4.3a and c, middle) differ by a factor of ~20, observations at B944 and B208 (Figure 4.3a and b, middle) differ by a factor of ~40, and observations at B944 and B206 (Figure4.3a and d, middle) differ by a factor of ~10. For engineering shear strain, observations at B944 and B950 (Figure 4.3a and c, bottom) differ by a factor of ~20, observations at B944 and B208 (Figure 4.3a and b, bottom) differ by a factor of ~10, and observations at B944 and B206 (Figure4.3a and d, bottom) differ by a factor of ~10.

Table 4.1 Estimated amplitudes for seiche event on 27 September 2014

		~78 minute component		*~51 minute component*		*~25 minute component*	
Lake Gauges		*Seiche load (cm)*	*RMSE*	*Seiche load (cm)*	*RMSE*	*Seiche load (cm)*	*RMSE*
GBD		8.2	0.16	1.1	2.9	0.3	2.92
PPN		3.3	0.31	0.1	2.4	0.1	2.4
SPN		0.1	0.9	1.1	0.5	0.1	0.9
Strainmeters		*Strain (ns)*	*RMSE*	*Strain (ns)*	*RMSE*	*Strain (ns)*	*RMSE*
B944	ε_A	12.4	1.8	0.8	4.7	1.1	4.7
	ε_D	11.8	2.1	0.5	4.7	1.0	4.7
	ε_S	32.4	1.6	3.5	11.5	1.6	11.5
B208	ε_A	2.5	2.1	3.1	2.3	1.0	2.5
	ε_D	0.2	0.5	1.3	0.6	0.8	0.7
	ε_S	2.1	0.5	0.3	0.9	0.2	0.9
B950	ε_A	8.1	10.9	6.2	6.2	3.2	6.5
	ε_D	0.7	0.8	0.2	0.5	0.2	0.5
	ε_S	1.2	1.3	0.6	0.8	0.4	0.8

The results suggest that the amplitude of a strain response due to a seiche wave is related both to the distance and azimuthal position relative to the lake. Even though both B950 and B206 are at similar distances from the lake B950 has higher measured values of areal strain (Figure4.3c, top) than B206 for comparable seiche load sizes (Figure4.3d, top). Similarly, the measured values of strain at B944 (Figure4.3a) are significantly larger than those measured at B208 (Figure4.3b) for the ~78 minute period even though they are both within 300 meters of the lake. The small ~78 minute component of the strain observed at B208 may be related to its position relative to the lake (Figure 2.1). B208 is in a location that is out of the direct path of the primary ~78 minute seiche wave (Figure 3.1), so the deformation due to this wave will not be as strong. This is supported by the spectral analysis of strain data from B208 during the large seiche events (Figure 4.1d, middle) that shows a strong ~51 minute period component that is associated with the seiche wave of the same period.

For ~78 minute period component at B950 and B208 there were several estimated strain amplitudes that were comparably larger than the strain measured during events of similar seiche wave amplitude (Figure 4.3, red circles), particularly for areal strain. These anomalously high values occur for seiche events on 2 November 2014, 15 March 2015, and 31 October 2015. We found that these anomalously higher values may correspond to the coupling of the borehole strainmeters to atmospheric pressure variations. During each of the three seiche events over the ~4 hour measurement window there are significant variations in atmospheric pressure that are semi-periodic, with a period of nearly 78 minutes. This semi-periodicity in the atmospheric pressure data lasts over the ~4 hour measurement window for these three events. We suggest that the changes in atmospheric pressure at this apparent ~78 minute period is supplementing the measured strain occurring at the ~78 minute period making the

estimated strain values anomalously high. In Figure 4.3a, we also highlight the same three events for B944, and as shown the measured values are not anomalously high (as it is for B208 and B950). This could be attributed to the relative size of the measurements between the strainmeters. Since the measured values of the strain at B944 are larger than those at B208 and B944, the atmospheric response of the strainmeters may be less noticeable. Additionally, the coupling of the individual strainmeters to atmospheric pressure may vary significantly between strainmeters (Table A.4).

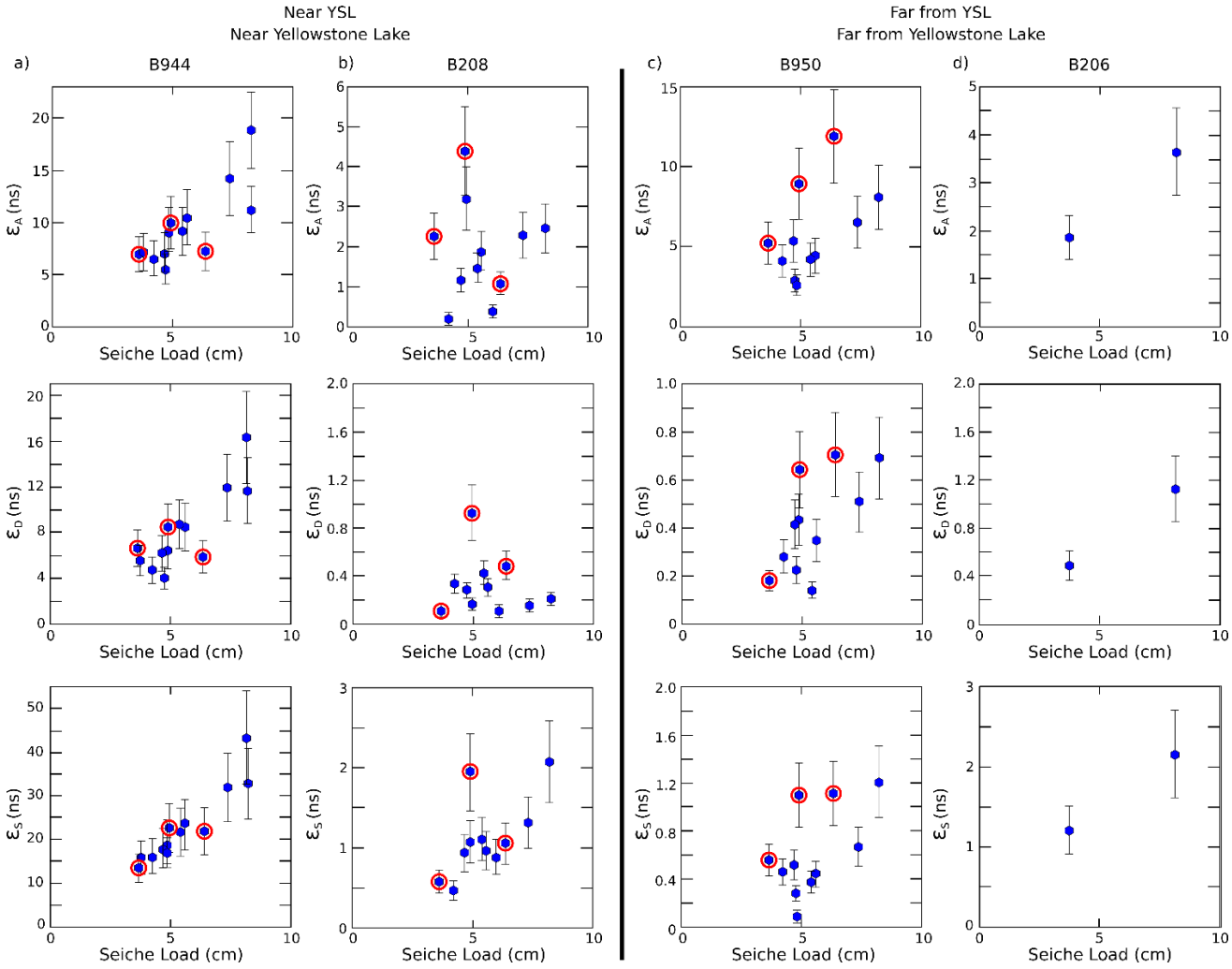

Figure 4.3: Areal (ε_A, top), differential (ε_D, middle), and engineering shear (ε_S, bottom) versus associated seiche load for the ~78 minute period component as measured during seiche events at (a) B944, (b) B208, (c) B950, (d) B206. Size of seiche load measurements from GBD are used. Each point represents a single seiche event. Error bars are ±25% the observed value to account for uncertainties in calibration of borehole strainmeter data. As discussed in the text, red circles indicate measured seiche events where there is significant atmospheric pressure interference.

For the ~51 minute period component the estimated amplitude of the seiche waves in the lake range between 0-1.2 cm at GBD (for 13 events, Table A.6), 0-0.6 cm at PPN (for 5 events, Table A.6), and 0.3-1.1 cm at SPN (for 5 events, Table A.6). For the 13 events observed at B944, the estimated

amplitude of areal strain ranges from 0.4-4.6 ns, differential strain from 0.6-5.6 ns, and engineering shear strain from 0.5-4.8 ns (Table A.8). For the 11 events observed at B208, the estimated amplitude of areal strain ranges from 0.8-3.8 ns, differential strain from 0.1-1.4 ns, and engineering shear strain from 0.1-0.7 ns (Table A.8). For the 11 events observed at B950, the estimated amplitude of areal strain ranges from 1.1-7.8 ns, differential strain from 0.1-0.7 ns, and engineering shear strain from 0.1-0.8 ns (Table A.8). For the 2 events observed at B206, the estimated amplitude of areal strain ranges from 0.4-0.6 ns, differential strain from 0.2-0.22 ns, and engineering shear strain from 0.4-0.5 ns (Table A.8).

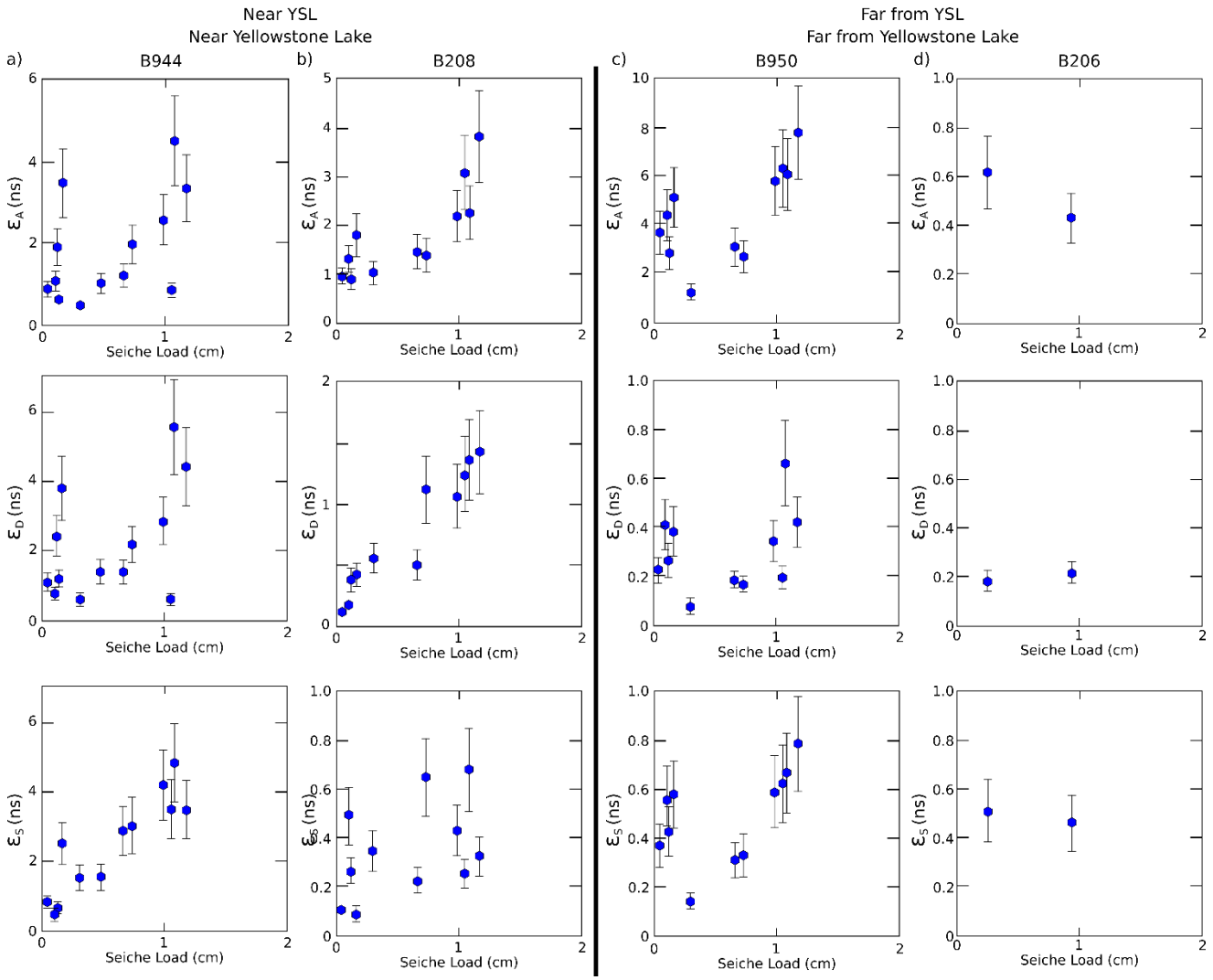

Figure 4.4: Areal (ε_A, top), differential (ε_D, middle), and engineering shear (ε_S, bottom) versus associated seiche load for the ~51 minute period component as measured during seiche events at (a) B944, (b) B208, (c) B950, (d) B206. Size of seiche load measurements from GBD are used. Each point represents a single seiche event. Error bars are ±25% the observed value to account for uncertainties in calibration of borehole strainmeter data

We examined the estimated areal (Figure 4.4, top row), differential (Figure 4.4, middle row), and differential engineering (Figure 4.4, bottom row) strains at each of the strainmeters compared with the

associated amplitude seiche wave with a ~51 minute period. In general the results suggest a linear relationship between seiche load size and strain response for each strain component at borehole strainmeters B944 (Figure 4.4a), B208 (Figure 4.4b), B950 (Figure 4.4c), and B206 (Figure 4.4d). However, there are anomalously high estimated values of strain at B944 and B950 for seiche loads ≤0.2cm. For Figure 4.4 we use measurements of the ~51 minute period seiche wave from GBD because it has the most complete record of seiche events. From spectral analysis we know that the ~51 minute period seiche wave component observed at GBD is not as strong as the ~78minute component. Therefore, these instances with the anomalously higher values could be attributed to the pressure gauge at GBD not measuring the correct amplitude of the associated seiche wave.

The estimated ~51 minute period areal strain at B950 (Figure 4.4c, top) is consistently larger than the areal strain measured at both B944 (Figure 4.4a, top) and B208 (Figure 4.4b, top) by a factor ~2. This is contrary to expectation, and observations of the ~78 minute period areal strain that the amplitude of the seiche induced strain should decrease with distance from the lake because it is farther from the source. Conversely, the estimated values of the differential and engineering shear strains at B950 (Figure 4.4c, middle and bottom), when compared to those at B944 (Figure 4.4a, middle and bottom) and B208 (Figure 4.4b, middle and bottom), do follow the expected relationship of decreasing amplitude with distance. This suggests two possibilities: 1) that even with calibration, the areal strain measured by B950 is not representative of true formation strain; or 2) that local conditions (i.e. weaker crust, higher temperatures, etc.) allow for significantly higher areal strains at B950.

For the ~25 minute period component the estimated amplitude of the seiche waves in the lake range between 0-0.6 cm at GBD (for 13 events, Table A.6), 0-0.4 cm at PPN (for 5 events, Table A.6), and 0.0-0.3 cm at SPN (for 5 events, Table A.6). For the 13 events observed at B944, the estimated amplitude of areal strain ranges from 0.2-2.0 ns, differential strain from 0.2-2.1 ns, and engineering shear strain from 0.2-2.4 ns (Table A.9). For the 11 events observed at B208, the estimated amplitude of areal strain ranges from 0.2-2.1 ns, differential strain from 0.1-0.8 ns, and engineering shear strain from 0.1-0.4 ns (Table A.9). For the 11 events observed at B950, the estimated amplitude of areal strain ranges from 0.5-3.20 ns, differential strain from 0.0-0.3 ns, and engineering shear strain from 0.1-0.4 ns (Table A.9). For the 2 events observed at B206, the estimated amplitude of areal strain ranges from 0.3-0.4 ns, differential strain from 0.0-0.1 ns, and engineering shear strain from 0.1-0.2 ns (Table A.9).

We examined the estimated areal (Figure 4.5, top row), differential (Figure 4.5, middle row), and differential engineering (Figure 4.5, bottom row) strains at each of the strainmeters against the associated amplitude seiche wave. For the ~25 minute period component, the linearity and self-consistency observed for the ~51 and ~78 minute period components begins to break down. However, it is still observed to some extent for observations at B944 (Figure 4.5a) and B208 (Figure 4.5b). This could be due to that the amplitudes related to the ~25 minute period are considerably small in both the lake (<1 cm) and strain (<3 ns). However, it can be observed again that the estimate areal strain amplitudes at B950 (Figure 4.5c) are equal to or larger than B208 (Figure 4.5b) or B944 (Figure 4.5a).

In summary, we were able to estimate the peak-to-trough amplitudes of the ~78, ~51, and ~25 minute periods components of both the seiche waves in Yellowstone Lake, and the associated strain response measured around the caldera. We found that the measured amplitude of the strain response (areal, differential, or engineering shear) measured at each borehole strainmeter was self-consistent and linearly proportional to the size of associated seiche wave. This comes from multiple seiche events of varying amplitudes over several years. The observed amplitude of the strain response at any given strainmeter varied depending its location, even between strainmeters at similar distances from Yellowstone Lake (i.e. B944 and B208 or B950 and B206). On a first order basis, this suggests that the amplitude of a strain response due to a seiche wave is related to both distance and azimuthal position relative to the lake

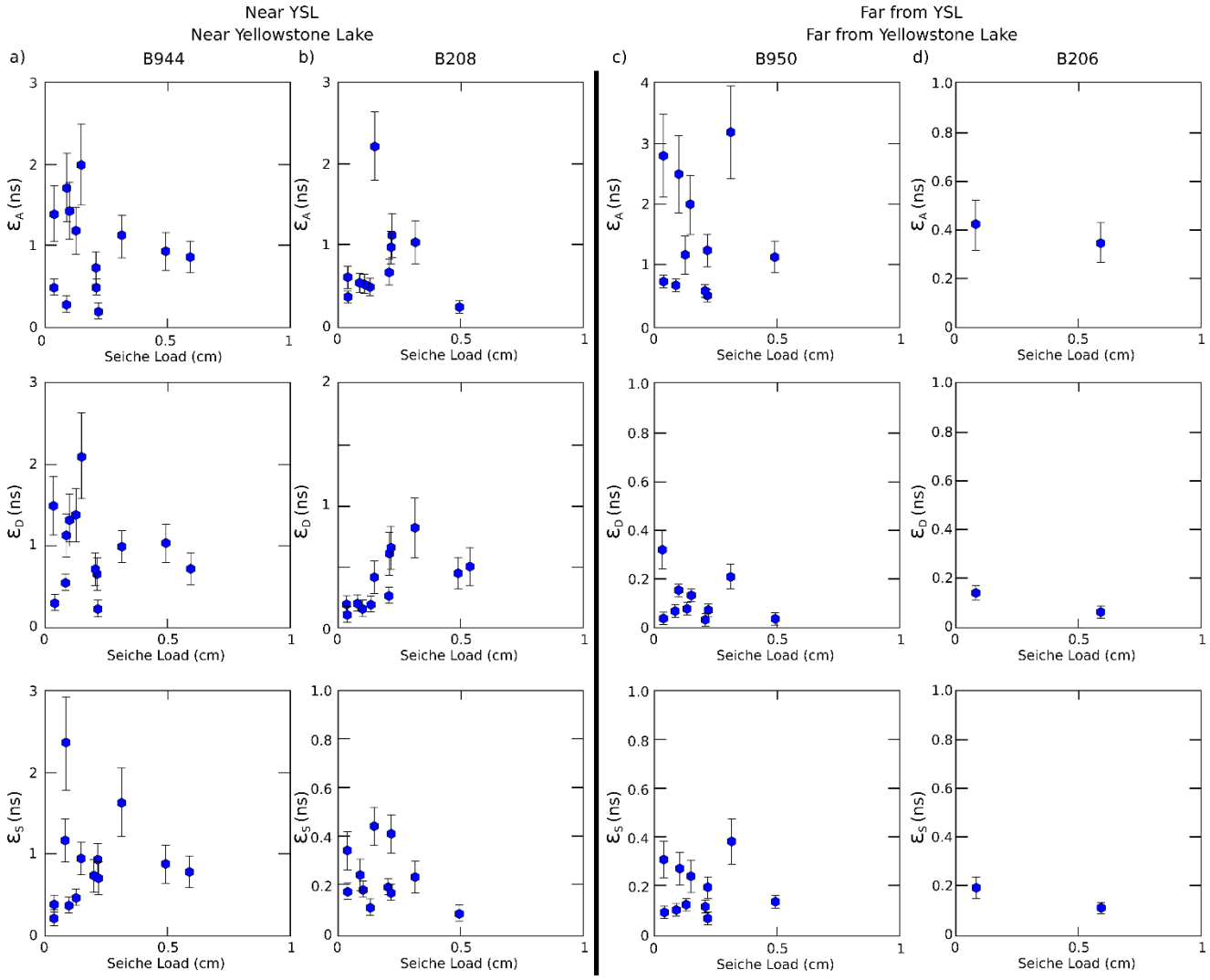

Figure 4.5: Areal (ε_A, top), differential ($\varepsilon_{D,}$ middle), and engineering shear strain ($\varepsilon_{S,}$ bottom) versus associated seiche load for the ~25 minute period component as measured during seiche events at (a) B944, (b) B208, (c) B950, (d) B206. Size of seiche load measurements from GBD are used. Each point represents a single seiche event. Error bars are ±25% the observed value to account for uncertainties in calibration of borehole strainmeter data

CHAPTER 5. MODEL EVALUATION AND INTERPRETAION

5.1 Two-layered viscoelastic model of the Yellowstone caldera

In general, strain can be related to an applied stress by the rheology of the material. Therefore if we have observations of the applied stress and the resultant strain we can begin to infer some of the rheological properties of the material. In the case of Yellowstone, the applied stress is the loading from the seiche waves in Yellowstone Lake and the resultant strain is the observed periodic strain response. How the subsurface strains vary spatially due to the same seiche load can therefore be related to the properties of the crust beneath the caldera surface.

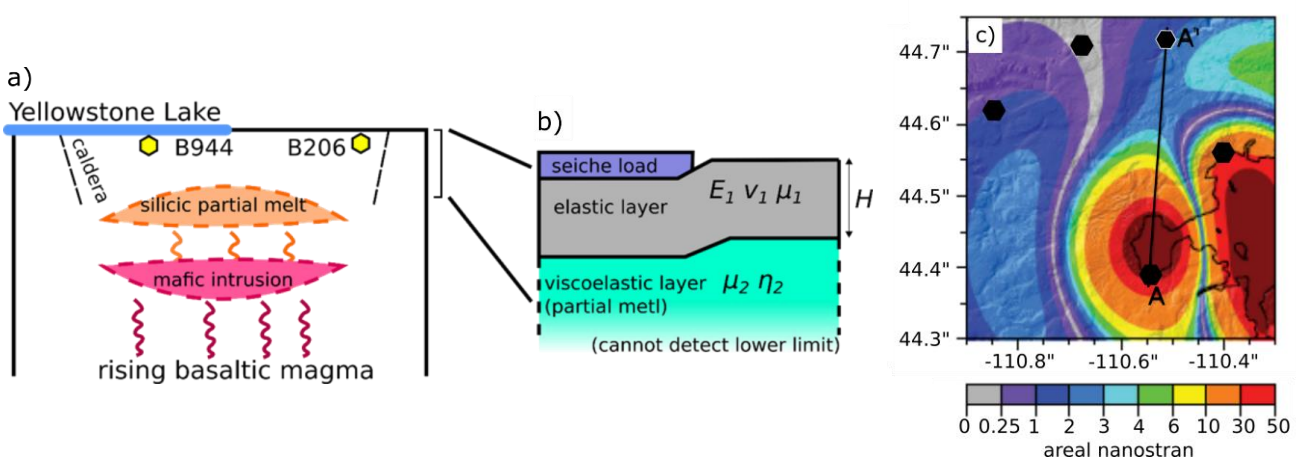

Figure 5.1: (a) Schematic cross section of the Yellowstone caldera, with approximate locations of Yellowstone Lake and borehole strainmeters. Model of the shallow subsurface rheology (b) with varying Young's modulus (E), Poisson's ratio (ν), shear modulus (μ), and depth to shallowest partial melt (H). After *Luttrell et al.* [2013]. (c) Modeled areal strain-field due to ~78 minute period seiche load in Yellowstone Lake for H=4 km, E_1=20 GPa, ν_1=0.25 and μ_2/μ_1=0.01

We constrain the subsurface properties by comparing the observed strain components at the borehole strainmeters against a strain-field produced by a geophysical model. The model we consider is composed of two layers, with an elastic layer on top of a viscoelastic half-space (Figure 5.1b). This two-layered model represents a solid upper crust overlying a partially molten body, which could be a larger magma reservoir (Figure 5.1a) or a small offshoot pocket of melt (<1 km in size). The model assumes that the bulk modulus of the two layers are the same so that the model can be fully described by four free parameters: the Young's modulus (E_1) and Poisson's ratio (ν_1) of the upper layer, the depth to the interface between the elastic and viscoelastic layers (H), and the ratio of their shear moduli (μ_2/μ_1) (Figure 5.1b). Previous research suggests that the modeled strain field does not vary significantly with changes in Poisson's ratio, so we hold Poisson's ratio at 0.25 reducing the number of free parameters to three [*Luttrell et al.*, 2013]. The modeled strain field in the caldera is calculated in response to a peak -to-trough seiche wave load using a semi-analytic method that convolves the real 2-D geometry of the surface load (described by Figure 3.1) with a vertical Green's function that describes the response of the subsurface to point load [*Luttrell and Sandwell*, 2010; *Luttrell et al.*, 2007; *B. Smith and Sandwell*, 2003; *Bridget Smith and Sandwell*, 2004] over the described combinations of material properties. This makes the relationship between an applied seiche load, and the resultant strain-field linear so we can scale the

modeled areal strain-field with our observed seiche wave amplitudes. Figure 5.1c shows what the modeled strain field looks like in the caldera due to the loading from the ~78 minute period seiche wave for one example set of rheological parameters.

5.2 Model constraints and interpretation

Section 4 described how all 3 frequencies of observed seiche waves contribute non-trivially to seiche-related deformation, and are therefore important for the complete characterization and understanding of this system. To date, however, only the shape of the ~78 minute seiche wave has been modeled (Figure 3.1) and used to generate calculated strain-field models [*Luttrell et al.*, 2013]. Therefore, for evaluating subsurface rheology and constraining our two-layered model parameters we only consider observations of the strain response associated with the ~78 minute period seiche wave.

Consider that the model space is a volume with axes equal the range of parameters Young's modulus (E_1), plate thickness (H), and shear modulus ratio (μ_2/μ_1) where each point within the volume is a modeled strain value. To constrain the model we compared the estimated strain response amplitude to the modeled strain-field value at the location of each of the borehole strain meters for each of the seiche events. We consider a set of parameters (H, E_1 and μ_2/μ_1) in model space to be a "fit" if the calculated strain (areal, differential, or engineering shear) value falls within ±25% of the estimated strain amplitude. As described in section 3.2, this range of ±25% is to account for the uncertainties in the calibration of borehole strainmeter data. Combined, the fit model parameters form a 3-D volume within model space.

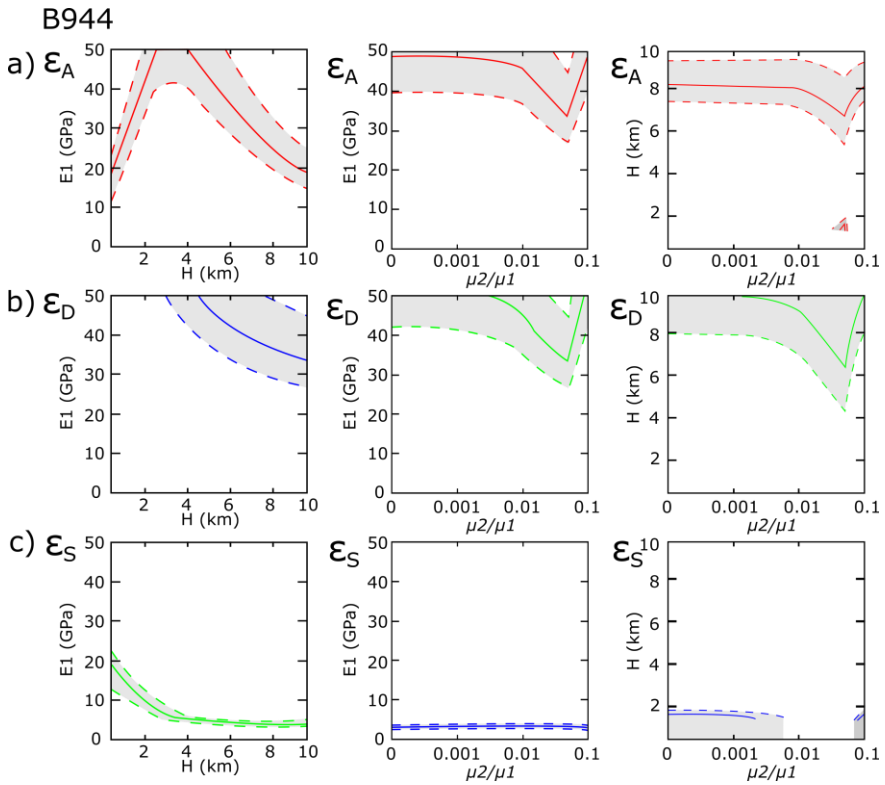

Figure 5.2: Model parameter space at B944 for (a) areal (ε_A,), (b) differential (ε_D,), and (c) engineering strain (ε_S). Observations of one seiche event used to constrain model space as a function of E_1 and (top) E_1 and H with $\mu 2/\mu 1$=0.1 and ν_1=0.25, (middle) E_1 and $\mu 2/\mu 1$ with H=7 km and ν_1=0.25, and (bottom) H and $\mu 2/\mu 1$ with E_1=35 GPa and ν_1=0.25. Contour values of observed strain (solid line) with error of ±25% (dashed line). Fit model space for the seiche event is shown (shaded grey).

Figure 5.2 shows 2-D slices of the 3-D model parameter space at B944 for areal (a), differential (b), and engineering strain. The contours in Figure 5.3 are the observed (solid) and the range (dashed) of the estimated strain amplitude for a single seiche event. From this we can see a visual representation of where in model space fits the observed values from three directions, E_1 versus H with μ_2/μ_1=0.1 (left), E_1 versus μ_2/μ_1 with H=7 km (center), and from three views, H versus μ_2/μ_1 with E_1=35 GPa (right). A set of parameters in model space that reproduces the observed strain will fall within the bounds of the contours (Figure 5.3, shaded grey regions). This would mean that for areal strain at B944 (Figure 5.3a) the combination of parameters H=6 km and E_1=40 GPa falls within the observed values, while H=4 km and E_1=20 GPa does not. Therefore for one seiche event areal strain (Figure 5.3a) only constrains $E_1 \geq$20 GPa, while H and μ_2/μ_1 are unconstrained. Differential strain (Figure 5.3b) constrains $E_1 \geq$25 GPa and $H \geq$3 while μ_2/μ_1 is unconstrained. Engineering shear strain (Figure 5.3c) constrains E_1 to ≥5 and ≤20 GPa, while H and μ_2/μ_1 are unconstrained. The constraints from a single strain component does not provide significant insight. Therefore we consider where each strain component (ε_A, ε_D, and ε_S) shares fit model space. Only the constrained model space from areal (Figure 5.2a) and differential (Figure 5.2b) strains have shared fit model space. So for one seiche event the overlap of model space of areal and differential strain constrains $E_1 \geq$25 GPa and $H \geq$3 km while μ_2/μ_1 is unconstrained. The constraints on the model from this one event suggest that in the region of B944 the upper crust in the caldera is weaker than a standard dry rhyolite (50-70 GPa [*Turcotte and Schubert*, 2002]) overlying partial melt as shallow as 3 km.

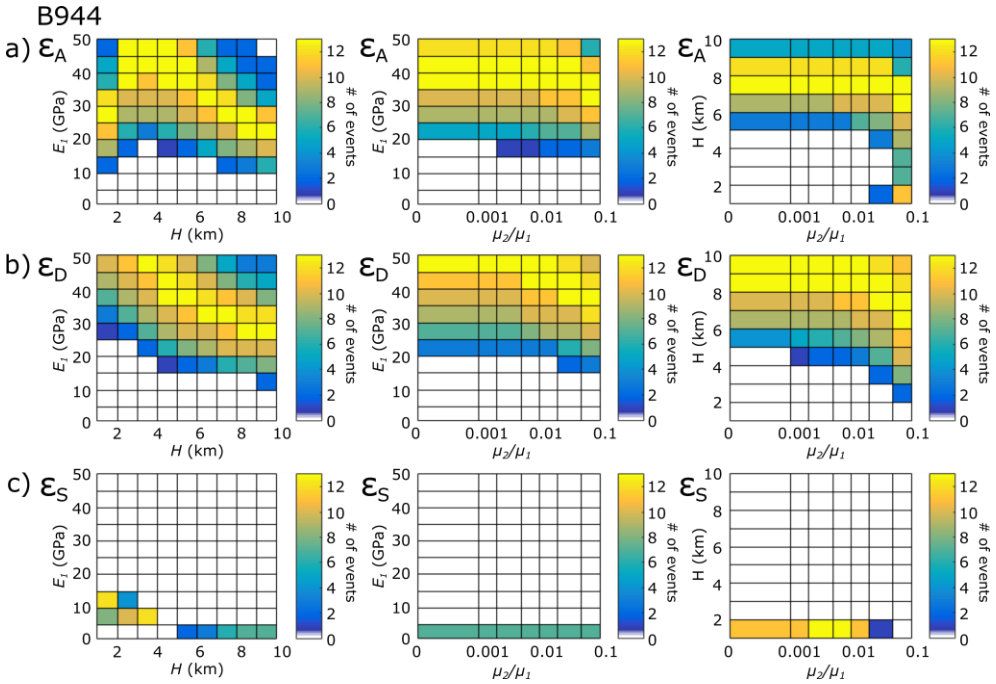

Figure 5.3: Model parameter space at B944 for (a) areal (ε_A,), (b) differential (ε_D,), and (c) engineering strain (ε_S). Observations from thirteen seiche events used to constrain model space as a function of (top) E_1 and H with $\mu 2/\mu 1$=0.1 and ν_1=0.25, (middle) E_1 and $\mu 2/\mu 1$ with H=7 km and ν_1=0.25, and (bottom) H and $\mu 2/\mu 1$ with E_1=35 GPa and ν_1=0.25. Warmer colors indicate more seiche events sharing fit model parameter space.

After we examined the constrained model space for one seiche event (Figure 5.2), we examined the constraints made for each of the measured seiche events at B944 (Figure 5.3). This is equivalent to taking all of the constrained model spaces for a single event (Figure 5.2, grey region) and stacking them together, and then determining the overlap in model space for multiple events. For areal, differential, and engineering shear strain constraints space there is a maximum of 12 of the 13 measured seiche events that have overlapping fit model parameter space. By comparing the fit model space for each seiche event we observed that there is a self-consistency for each strain component (Figure 5.3a, b, and c). Meaning that seiche events with different amplitude seiche loads and strain responses consistently constrained similar model space. In Figure 5.3 the warmer colors indicate more events with similar constrained model space.

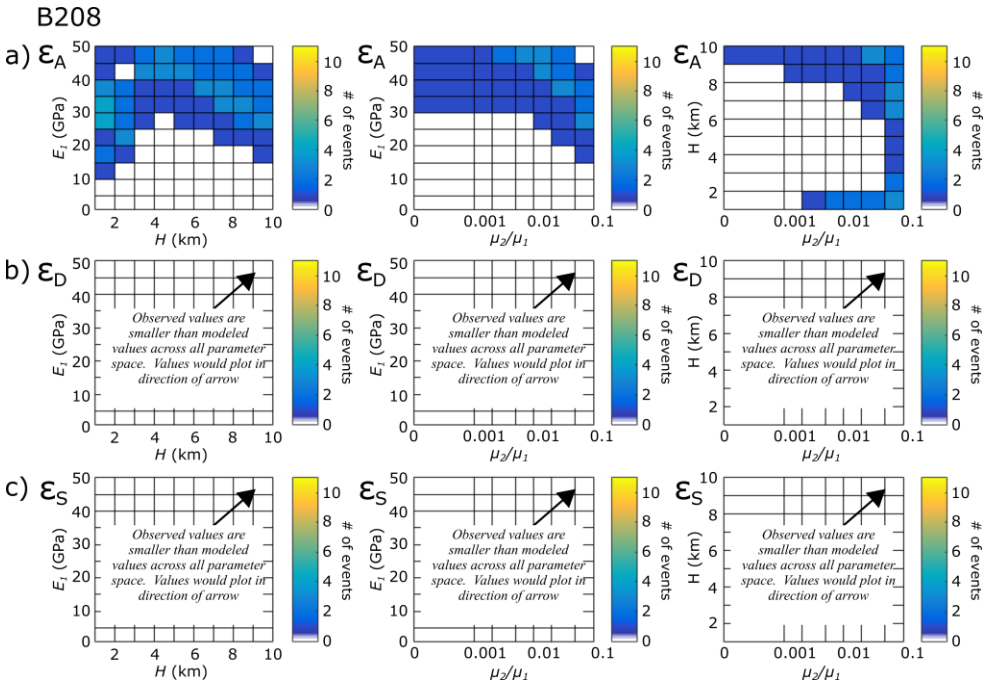

Figure 5.4: Model parameter space at B208 for (a) areal (ε_A,), (b) differential (ε_D,), and (c) engineering strain (ε_S). Observations from thirteen seiche events used to constrain model space as a function of (top) E_1 and H with $\mu 2/\mu 1$=0.01 and ν_1=0.25, (middle) E_1 and $\mu 2/\mu 1$ with H=4 km and ν_1=0.25, and (bottom) H and $\mu 2/\mu 1$ with E_1=15 GPa and ν_1=0.25. Warmer colors indicate more seiche events sharing fit model parameter space.

As we examined the combined constrained model space for the areal strain (Figure 5.3a) it was found that as μ_2/μ_1 went from 0 to 0.1, the constraints of E_1 approached 25 GPa and H went to 1 km. In other words, as the lower layer goes from a complete fluid (μ_2/μ_1=0) to more viscous ($\mu_2/\mu_1 \geq 0.1$), the rigidity of the elastic layer (E_1) decreases asymptotically to 20 GPa and the depth (H) to the viscous layer decreased to ~1km. This means that thicker weaker plate fits just as well as a thinner stiffer one. For the combined model space constrained by differential strain (Figure 5.3b) we found that as μ_2/μ_1 went from 0 to 0.1, the constraints of E_1 approached 30 GPa and H went to 4 km. For the combined model space constrained by engineering strain (Figure 5.3c) we found that as μ_2/μ_1 went from 0 to 0.1, E_1 approached 10 GPa and H constrained $\leq$4 km. For areal, differential and engineering shear μ_2/μ_1 was unconstrained. When we compare the overlap of fit model parameter space between the areal and differential strain the

combined observed values constrain $E_1 \geq 30$ GPa and $H \geq 4$ km while μ_2/μ_1 is unconstrained. These results suggest that local to B944 the stiffness of the upper crust near the lake to be at least 30 GPa overlying partially molten material as shallow as 4 km.

At B208, for all of the measured seiche events (11 events) no observed values of differential (Figure 5.4b) or engineering shear (Figure 5.4c) strain could constrain available model parameter space. The measured values of differential and engineering shear strain are consistently smaller than any of the modeled values. However, for areal strain 6 out of 11 measured seiche events consistently constrained similar model space (Figure 5.4b, c, and d, top). We found that as μ_2/μ_1 went from 0 to 0.1, E_1 approached 15 GPa while H remained unconstrained. With the absence of constrained model space from differential or engineering strain, further refinement of the constraints at B208 is difficult. However, the areas of model space that are constrained by the observations of areal strain at B208 (Figure 5.4, top) are similar to those constrained by B944 (Figure 5.3, top). It is possible that this is because both B208 and B944 are both close to the lake (<300m) and therefore the local structure and rheology around them in similar.

For all of the measured seiche events at B950 (11 events) no observed values of areal strain (Figure 5.5a) constrain model space. The measured values of areal strain are consistently larger than any of the modeled values. However, for differential (Figure 5.5b) and engineering shear (Figure 5.5c) strain up to 8 out of 11 measured seiche events consistently constrained similar model space.

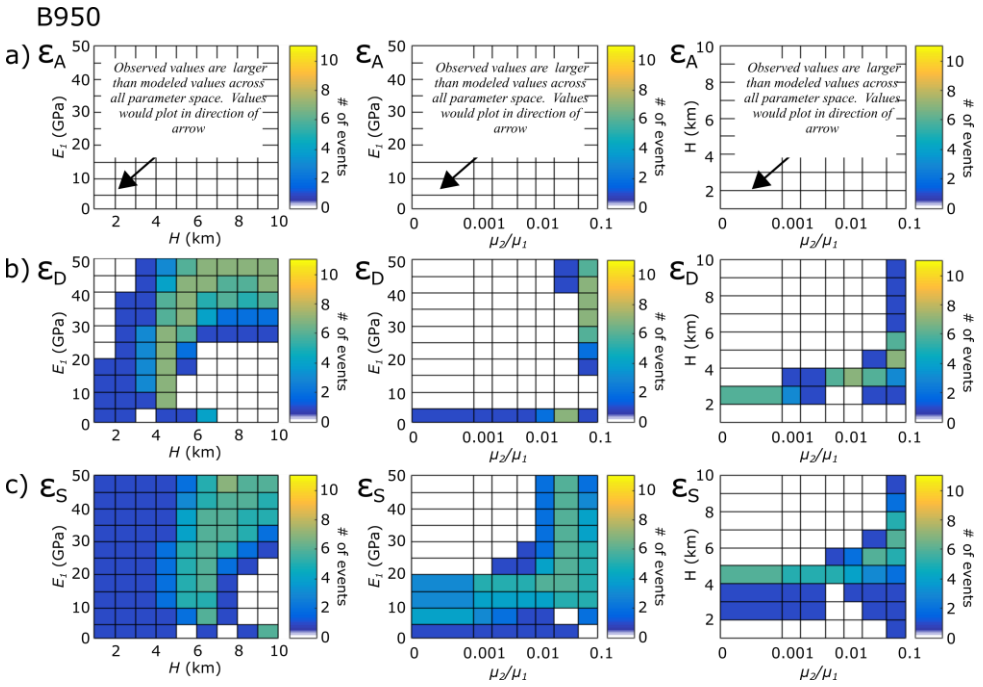

Figure 5.5: Model parameter space at B950 for (a) areal (ε_A,), (b) differential (ε_D,), and (c) engineering strain (ε_S). Observations from thirteen seiche events used to constrain model space as a function of (top) E_1 and H with $\mu 2/\mu 1$=0.01 and ν_1=0.25, (middle) E_1 and $\mu 2/\mu 1$ with H=4 km and ν_1=0.25, and (bottom) H and $\mu 2/\mu 1$ with E_1=15 GPa and ν_1=0.25. Warmer colors indicate more seiche events sharing fit model parameter space.

As we examined the combined constrained model space for the differential strain (Figure 5.5, middle) it was found that as μ_2/μ_1 went from 0 to 0.1, E_1 is constrained to ≥10 GPa and H is constrained to ≥2 km. In other words, as the lower layer goes from a complete fluid (μ_2/μ_1=0) to more viscous ($\mu_2/\mu_1 \geq 0.1$) the rigidity of the elastic layer (E_1) decreases asymptotically to 10 GPa and the depth (H) to

the viscous layer is greater than 2 km. For the combined model space constrained by engineering shear strain (Figure 5.5, bottom) we found that as μ_2/μ_1 went from 0 to 0.1, E_1 remained greater than 10 GPa and H went to 3 km. Individually, observations of differential strain and engineering shear strain do not constrain μ_2/μ_1. When we compare the overlap of fit model parameter space between the differential and engineering shear strain the combined observed values constrain $E_1 \geq 15$ GPa, H=3-6 km, and $\mu_2/\mu_1 \geq 0.02$. These results suggest that local to B950 the stiffness of the upper crust far the lake to be at least 15 GPa overlying partially molten material as shallow as 3 km.

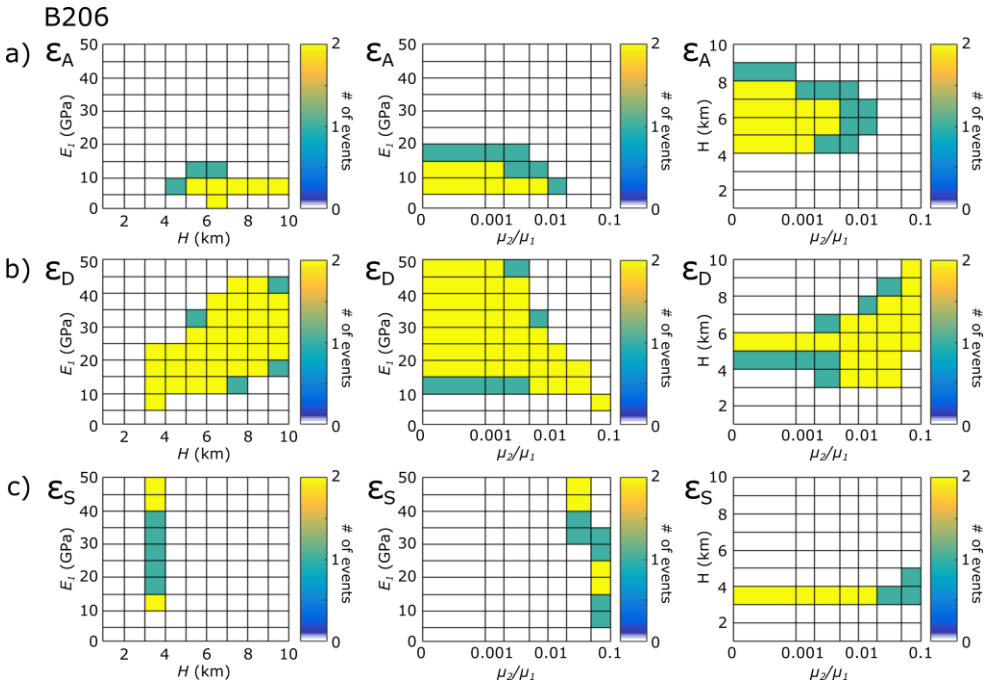

Figure 5.6: Warmer colors indicate more seiche events sharing fit model parameter space. Model parameter space at B206 for (a) areal (ε_A,), (b) differential (ε_D,), and (c) engineering strain (ε_S). Observations from thirteen seiche events used to constrain model space as a function of (top) E_1 and H with $\mu 2/\mu 1$=0.01 and ν_1=0.25, (middle) E_1 and $\mu 2/\mu 1$ with H=4 km and ν_1=0.25, and (bottom) H and $\mu 2/\mu 1$ with E_1=15 GPa and ν_1=0.25. Warmer colors indicate more seiche events sharing fit model parameter space.

We found that for both of the measured seiche events at B206 the model space constrained by observations of the areal (Figure 5.6a), differential (Figure 5.6b), and engineering shear (Figure 5.6c) strains to be self-consistent. As we examined the combined constrained model space for the areal strain (Figure 5.6a) it was found that as μ_2/μ_1 went from 0 to 0.1, E_1 is constrained to between 10-15 GPa and H is constrained to ≥4 km. For the combined model space constrained by differential strain (Figure 5.6b) we found that as μ_2/μ_1 went from 0 to 0.1, E_1 was constrained to ≥10 GPa and H ≥2 km. For the combined model space constrained by engineering shear strain (Figure 5.6c) we found that as μ_2/μ_1 went from 0 to 0.1, E_1 was constrained to ≥10 GPa and H ≥3 km. Individually, observations of the strain components do not constrain μ_2/μ_1. When we compare the overlap of fit model parameter space between all three strain components the combined observed values constrain E_1 =10-15 GPa, H=3-5 km, and $\mu_2/\mu_1 \leq 0.01$. These results suggest that local to B206 the stiffness of the upper crust far from the lake to be 10-15 GPa overlying partially molten material as shallow as 3 km.

To summarize, we found that the two-layered viscoelastic half-space model was capable of reproducing strain values within the observed ranges for at least one strain component at each of the borehole strainmeters. The combination of model parameters that fit the observed strain values was consistent across multiple seiche events per strain component for each strainmeter. This includes cases where the constraints are outside of current model parameter space (i.e. B950, areal strain; B208, differential and engineering strain). The results indicate a distinct difference between the constrained model space from borehole strain meters near the lake (B944 and B208) and far away (B950 and B206). In general, the observations from B944 and B208 suggest a thicker (H=4-8 km) and more rigid ($E_1 \geq 30$ GPa) upper elastic layer. Conversely, constraints from B950 and B206 suggest a thinner (H=3-5 km) and weaker (E_1=10-20 GPa) upper elastic layer. This suggests that closer to the lake (B944 and B208) there is partially molten material at slightly greater depths under a stiffer crust than across the caldera (B950 and B206).

CHAPTER 6. FROM TIME DIFFERENCE TO VISCOSITY

6.1 Relating the viscosity of a viscoelastic solid to relaxation time

To constrain the viscosity (η) of the melt (thereby melt percentage) in the subsurface we needed to first constrain the shear modulus of the subsurface and the relaxation time (τ_m). Mathematically, a viscoelastic material is identical to an elastic material with an effective shear modulus that decays over time from an initial value (μ, equation 4).

$$\mu_1(t) = \mu\left(\frac{e^{\frac{t}{\tau_m}}}{2-e^{\frac{t}{\tau_m}}}\right) \tag{4}$$

Constraints on the shear modulus ratio can be used to determine t/τ_m, where τ_m (relaxation time) can be related to the viscosity and shear modulus of the unrelaxed material (equation 5).

$$\eta = \tau_m \frac{\mu_1}{2} \tag{5}$$

If the elastic and viscoelastic layers are composed of the same material (i.e. rhyolite) and only differ by the viscosity then the shear modulus can be computed by equation (6) using the constraints on E_1 and v_1

$$\mu_1 = \frac{E_1}{2(1+v_1)} \tag{6}$$

Substituting equation (6) into (5) we can relate the viscosity to E_1 and v_1 (equation 7).

$$\eta = \frac{\tau_m E}{4(1+v)} \tag{7}$$

Since we had constraints on E1 and v1, we needed estimates of how much time it took to relax the material to the constrained μ_2/μ_1 value. However, in the absence of strong constraints on μ_2/μ_1 we assume that full relaxation occurs within the observed time difference between signals. We consider a material to be fully relaxed after ~4 τ_m when the effective shear modulus (μ_1) has decayed to 1% of its initial value, after equation (4) [*Luttrell and Sandwell*, 2010].

6.2 Estimating relaxation time by time difference of phase and onset time

The first step in determining the relaxation time is to determine the phase difference or time delay between when a strain response is observed at a borehole strainmeter relative to when seiching begins in the lake. In prior research the phase difference (or lack thereof) was determined by examining the difference in onset time between when a seiche is measured at the lake gauge, and then when the associated strain response is observed at a borehole strainmeter [*Luttrell et al.*, 2013]. However, the atmospheric coupling of the borehole strainmeters interferes with the ability to determine the absolute onset time of the seiche related strain response, especially during the first ~1 hour after onset. Therefore, we address this by comparing the time difference directly between the strain response signals after the seiching has been established. We compared the direct signals so we can use any patterns or periodic behaviors in the time series to best match up associated peaks and curves. We found that consistently the peak of the strain response at B944 (Figure 6.1, red) preceded that of the closest pressure gauge in the lake GBD (Figure 6.1, blue) by several minutes. This could be because the strainmeter is measuring

the strain due to the seiching in West Thumb basin before the lake pressure gauge can make the corresponding measurement of the lake level. Therefore, we used B944 as the best reference for measurements of time delay between the other strainmeters.

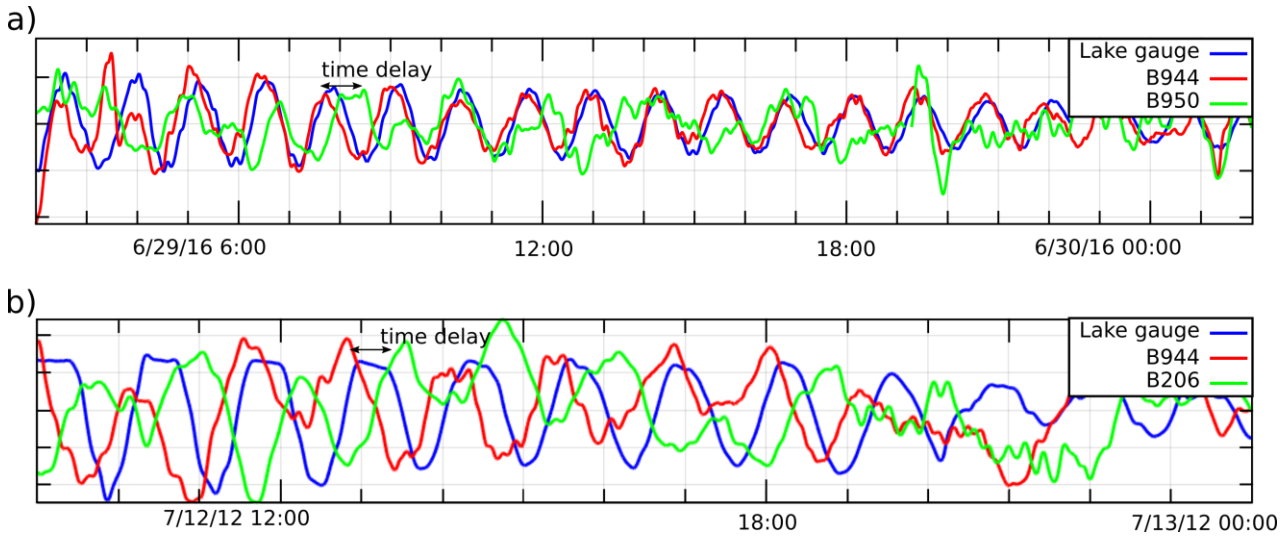

Figure 6.1: Filtered and normalized time series data over a day for seiche events occurring on (a) 29 June 2016 and (b) 15 March 2015. (a) Lake pressure gauge GBD (blue) and areal strain as measured on bore hole strainmeters B944 (red) and B950 (green) are shown. (b) Lake pressure gauge GBD (blue) and areal strain as measured on bore hole strainmeters B944 (red) and B206 (green) are shown. Arrow bar indicates the time difference between measurements of areal strain.

We determined the range of time differences for each possible measured seiche event between observations at B944 and B206 (two events), and B944 and B950 (11 events). We only consider observations at B950 and B206 because they are most sensitive to the structural and rheological properties between them and the Lake. The range of time differences can be converted to relaxation time by dividing the observed the time differences by 4.

We recorded the time difference between peaks (Figure 6.1) of the strain signals with respect to a seiche event measured at B944. The time difference between peaks at B950 with respect to B944 for multiple events ranges from ~7–60 minutes (τ_m=~1.75-15 minutes) for areal strain, ~5–60 minutes (τ_m=~1.25-15 minutes) for differential strain, and ~6-60 minutes (τ_m=~1.5-15 minutes) for engineering strain (Table 6.1).. The time difference between peaks at B206 with respect to B944 for multiple events ranges from ~ 45 minutes (τ_m=~11.25 minutes) for areal strain, ~25–40 minutes (τ_m=~6.25-10 minutes) for differential strain, and ~28-42 minutes (τ_m=~7-10.5 minutes) for engineering strain (Table 6.1).

The results from the time difference between B944 and B950 almost cover the full spectrum of possibilities for a ~78 minute period signal. This means that for all the events at B950, the signals range from being nearly in phase to completely out of phase. Similarly, we found that the strain response signals between B944 and B206 are also either roughly in phase, or out of phase. Therefore considering observations of phase do not constrain possible relaxation times.

Since the estimates from time difference are inconsistent we digressed to considering onset time of a seiche event between strainmeters to make viscosity estimates. However, as discussed it is difficult to determine the absolute onset time because of the atmospheric pressure coupling of borehole strainmeters. We considered the time between when we see the onset of the atmospheric pressure response in the strainmeter data and then when seiching can initially be observed. This is because the

onset of seiching must occur at some point during that time. Observations of this suggest onset time of seiche events at B950 to occur within 1 hour ($\tau_m \leq 15$ minutes) of onset at B944 and within 25 ($\tau_m \leq 6.25$ minutes) minutes at B206.

Table 6.1: Measured time difference between filtered time series

	B944 to B950			B944 to B206		
Seiche Event	*Strain*	*Est. Time dif. (min)*	*Relaxation Time (min)*	*Strain*	*Est. Time dif. (min)*	*Relaxation Time (min)*
26 August 2011	ε_A	--	--	ε_A	45	11.25
	ε_D	--	--	ε_D	40	10.0
	ε_S	--	--	ε_S	42	10.5
12 July 2012	ε_A	--	--	ε_A	45	11.25
	ε_D	--	--	ε_D	25	6.25
	ε_S	--	--	ε_S	28	7
27 September 2014	ε_A	7	1.75	ε_A	--	--
	ε_D	22	5.5	ε_D	--	--
	ε_S	33	8.25	ε_S	--	--
26 October 2014	ε_A	27	6.75	ε_A	--	--
	ε_D	26	6.5	ε_D	--	--
	ε_S	22	5.5	ε_S	--	--
2 November 2014	ε_A	15	3.75	ε_A	--	--
	ε_D	12	3.0	ε_D	--	--
	ε_S	14	3.5	ε_S	--	--
22 December 2014	ε_A	37	9.25	ε_A	--	--
	ε_D	32	8.0	ε_D	--	--
	ε_S	37	9.25	ε_S	--	--
15 March 2015	ε_A	27	6.75	ε_A	--	--
	ε_D	18	4.5	ε_D	--	--
	ε_S	27	6.75	ε_S	--	--
5 August 2015	ε_A	25	6.25	ε_A	--	--
	ε_D	20	5.0	ε_D	--	--
	ε_S	25	6.25	ε_S	--	--
31 October 2015	ε_A	50	12.50	ε_A	--	--
	ε_D	40	10.0	ε_D	--	--
	ε_S	34	8.5	ε_S	--	--
22 May 2016	ε_A	60	15.0	ε_A	--	--
	ε_D	60	15.0	ε_D	--	--
	ε_S	60	15.0	ε_S	--	--

(Table 6.1 Continued)

Seiche Event	B944 to B950 Strain	Est. Time dif. (min)	Relaxation Time (min)	B944 to B206 Strain	Est. Time dif. (min)	Relaxation Time (min)
29 June 2016	ε_A	32	8.00	ε_A	--	--
	ε_D	27	6.75	ε_D	--	--
	ε_S	26	6.5	ε_S	--	--
15 August 2016	ε_A	7	1.75	ε_A	--	--
	ε_D	-5	-1.25	ε_D	--	--
	ε_S	-6	-1.50	ε_S	--	--
5 September 2016	ε_A	27	6.785	ε_A	--	--
	ε_D	20	5.0	ε_D	--	--
	ε_S	23	5.75	ε_S	--	--

6.3 Estimation of viscosity by relaxation time

To determine potential ranges for the viscosity of the lower layer we must consider both the constraints on elastic moduli from the model evaluation and temporal observations of the relaxation time. In a Maxwell viscoelastic solid the viscosity (η) can be related to the relaxation time (τ_m) and the shear modulus (μ) (equation 5). With a shear modulus ratio of zero, the model is equivalent to an elastic plate over top an inviscid fluid, so therefore the relaxation time will be zero (instantaneous response), implying that the phase difference between the applied seiche load and the strain response will be zero. As the shear modulus ratio increases (increasing viscosity of the bottom layer) the relaxation time increases, thereby increasing the phase difference between the applied seiche load and the strain response. The shear modulus is related to Young's modulus and the Poisson's ratio (equation 6). Furthermore we can then relate the viscosity of the lower layer to the relaxation time, the Young's modulus (E_1), and the Poisson's ratio (v_1) (equation 7).

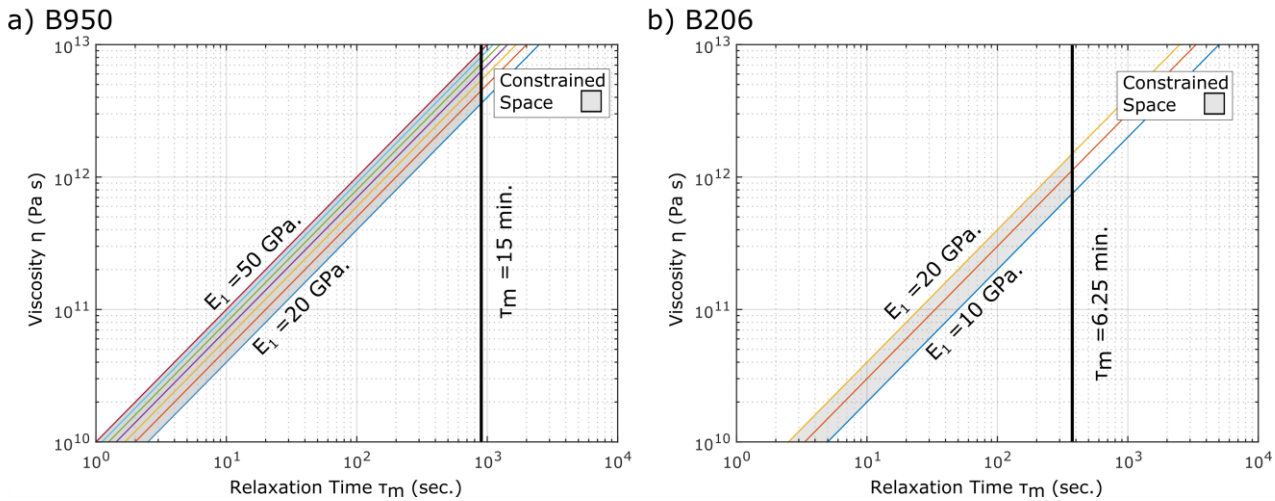

Figure 6.2: Viscosity versus relaxation time calculated using constrained Young's modulus (colored lines) at (a) B950 and (b) B206. Young's moduli values are in steps of 5. Estimated relaxation times from time series indicated by black line. Constrained viscosities indicated by shaded grey region.

Though standard relations of elastic properties the shear modulus can be approximated using the

constraints of the Young's modulus from the previous subsection (equation 5). With constraints on the shear modulus (Section 5) and the relaxation time (Section 6.1) we can make estimates of the viscosity by the relationship of equation (7). From these relations it estimates the viscosity of the lower later to $\leq 10^{13}$ Pa s and $\leq 10^{12}$ Pa s at B950 (Figure 6.2a) and B206 (Figure 6.2b) respectively.

CHAPTER 7. DISCUSSION

7.1 Structural and rheological implications for the subsurface

To summarize, we found that the two-layered viscoelastic half-space model was capable of reproducing strain values within the observed ranges for at least one strain component at each of the borehole strainmeters. The combination of model parameters that fit the observed strain values was consistent across multiple seiche events per strain component for each strainmeter. This includes cases where the constraints are outside of current model parameter space (i.e. B950, areal strain; B208, differential and engineering strain). Results indicated that for observations near Yellowstone Lake (B944 and B208) as the lower layer went from a complete fluid (μ_2/μ_1=0) to being more viscous (μ_2/μ_1=0.1) it decreased the plate thickness (H) and Young's modulus (E_1). Conversely, for observations far from Yellowstone Lake (B950 and B206) as the lower layer went from a complete fluid (μ_2/μ_1=0) to being more viscous (μ_2/μ_1=0.1) it increased the plate thickness (H) and did not affect Young's Modulus (E_1). Additionally, the results show a distinct difference between the constrained model space from borehole strain meters near the lake (B944 and B206) and far away (B950 and B206). In general, the observations from B944 and B208 suggest a thicker (H=4-8 km) and more rigid ($E_1 \geq$30 GPa) upper elastic layer. Conversely, constraints from B950 and B206 suggest a thinner (H=3-5 km) and weaker (E_1=10-20 GPa) upper elastic layer.

There is a difference in the constraints made on the model space between the different strainmeters in the caldera. This difference is most distinct when we examine the constraints made from borehole strainmeter observations made near Yellowstone Lake (B944 and B208) and those far away (B950 and B206). Typically we found that observations from B944 and B208 suggest a thicker (H=4-8 km) and more rigid ($E_1 \geq$30 GPa) upper elastic layer. Conversely, constraints from B950 and B206 suggest a thinner (H=3-5 km) and weaker (E_1=10-20 GPa) upper elastic layer. We interpret these results to reflect laterally heterogeneous rheology and structure of the subsurface. While the model itself is not laterally heterogeneous, we constrain it at individual points (the borehole strainmeters). This means that the constraints made on model space by strainmeter are indicative of the local area around the strainmeter. Results indicate that the upper limits of the magma reservoir is constrained to deeper near the lake (~4-8 km) than further away (~3-5 km). This could also indicate that smaller pockets of melt such as sills or dikes are at different depths within the caldera.

These results are consistent with research that estimates the depth to the magma reservoir between 3 – 10km [*Chu et al.*, 2010; *DeNosaquo et al.*, 2009; *Husen et al.*, 2004; *Miller and Smith*, 1999; *Seats and Lawrence*, 2014]. The spatial difference in the constraints made by this research is consistent with research interpreting crystallizing magma to be located at shallowing depths along the north and northwestern boundary of the caldera (near B206 and B950) and at greater depths in the southeast (near B944 and B208 [*Chu et al.*, 2010]. B950 and B206 are also located near what is interpreted from seismic tomography as upwelling magma beneath the resurgent domes [*Lowenstern et al.*, 2006]. If this is the case then there could be shallow melt bodies in place. Additionally the strength of the solid upper crust varies spatially from proximal (E_1=25–50 GPa) to distal (E_1=10-15 GPa) from the lake. A cold dry rhyolite will typically have a Young's modulus of 40-70 GPa [*Turcotte and Schubert*, 2002]. In Yellowstone, the dominant rheology is rhyolite which may be thermally weakened [*Christiansen et al.*, 2007]. The weaker upper crust in the north section of the caldera (near B950 and B206) is consistent with the implications of a shallower melt in the region.

7.2 Viscosity to melt percentage

The constraints from the temporal observations (τ_m) and Young's Modulus (E_1) constrain the viscosity of the lower layer to $\leq 10^{13}$ and $\leq 10^{12}$ Pa s beneath B950 and B206 respectively. A fully molten rhyolitic melt typically has a viscosity ~10^5-10^8 Pa s. Near melting point rhyolitic rocks have a viscosity ~10^{16} Pa s [*Ardia et al.*, 2008]. The results from this research therefore suggest that the lower layer is partially molten. This is consistent with the results presented by *Luttrell et al.* [2013]. The viscosity of a multiphase magma is dependent on the composition, the temperature, water content, the strain rate, and the crystal fraction of the melt [*Petford*, 2003]. In a Yellowstone caldera rhyolite a viscosity 10^{12}-10^{13} Pa s likely corresponds to a mush with 30-40% melt fraction. This fraction may vary depending on the volatile content.

7.3 Discrepancy between the observed and modeled strain

The model used here is capable of reproducing strain-field values that fall within the range of the observed values across multiple seiche events from each of the borehole strainmeters. However, there is a discrepancy in constrained model space between strain components for three of the four borehole strainmeters. For B944 the constraints made by observations of the engineering strain are significantly different than the constraints of the areal or differential strain. Observations of differential and engineering strain at B208 provide no constraints on model space within the current parameter ranges. Similarly, this is the case for the areal strain observations at B950.

For the calculated strain-field, the strain gradient is relatively large near the source of the load (Figure 5.1c). This means that close to the lake, subtle variations in the load shape could alter the computed strain-field more compared to further away. This effect of the model could account for the discrepancies between the fit model parameter spaces between the strain components at B944. The modeled shape of the seiche load used in the computation of the strain-field is based on the bathymetry of Yellowstone Lake. Depending on the shape of the seiche wave and how it loads the crust it may cause more shearing strain than uniform compression in the caldera, or vice versa.

Variations in the modeled shape of the ~78 minute period load may not account for all the observations at B208. From the results presented in this research it was found that the seiche induced strain at B208 has a stronger correlation to observations of the ~51 minute period seiche taken at SPN. Given the proximity of B208 to SPN, this relationship is expected. This ~51 minute period seiche could correspond to water mass movement from the central basin to the south and south east arms. The model used for this research only accounts for strain caused by the ~78 minute period seiche. Therefore a step for further research would be to examine the modeled strain-field due to the ~51 minute seiche load shape. This could reconcile the discrepancies observed for B208, and make the observations from further research more robust. However, this would require more direct lake observations from the central basin and Southeast Arm of Yellowstone Lake.

At B950 the observed values of the areal strain across all seiche events is significantly higher than the modeled values for all combinations of model parameters. There are three main possibilities that could account for this discrepancy. First, it has been well documented that the borehole strainmeters in Yellowstone have significant vertical coupling related to atmospheric pressure. This coupling has the largest effect on the measured areal strain. Those that regularly work with these strainmeters propose that the measured areal strain is really an apparent areal strain that is related to the vertical coupling [*Hodgkinson et al.*, 2013; *Roeloffs*, 2010]. It is argued that observations of apparent areal strain must be carefully considered before drawing conclusions. This is plausible since the measured values of areal strain are an order of magnitude larger than either the differential or engineering strain. A second possibility is that even with calibration, the areal strain measured at B950 is not representative of true formation areal strain. As we observed from our analysis the areal strain amplitudes associated with the

~78 and ~51 minute period seiche waves measured at B950 were comparable to or larger than those at B208 for similar size seiche waves. Similarly, the estimated amplitude of areal strain at B950 was consistently larger than areal strain measured at B206, even though they are at similar distances (>20 km).

7.4 Limitations of borehole strainmeters

Borehole strainmeters are sophisticated geophysical instruments capable of measuring incredibly minute deformation with a precision of ~ 0.05 nanostrain. However, the functional precision of these instruments may be higher. This reliability is dependent on the ground noise present in the region of the borehole and the time duration of the phenomena being studied. Seismic signals are frequently measured on the order of 0.1 nanostrain. Daily changes in local strain (apart from Earth tides) are on the order of ~1 nanostrain. These regular changes can limit the useful sensitivity to ~1 nanostrain [*Gladwin*, 1984]. Several observations of differential and engineering shear strain measured at B950 fall below the useful sensitivity of ~1 ns, even for the largest amplitude seiche events (7 cm). While it is important to consider the useful sensitivity of borehole strainmeters we suggest that we can reliably measure sub nanostrain transients that are representative of seiche related deformation. The defining characteristic of the strain measurements in this research is that they have consistent, long period (~78, ~51, ~25 minutes) that distinguishes them from both seismic and diurnal variations. Also, it is important to consider that for our measurements we are only interested in relative changes in the observed strain. It can be observed in our results that measurements of strain less than ~1 ns at B950 are self-consistent and follow a linear relationship for the ~78 (Figure 4.3c) and ~51 (Figure 4.4c) minute period components. The observed relationship would not be self-consistent or linear if the useful sensitivity was truly interfering with the measurements of seiche induced strain.

The subsurface environment in Yellowstone is not ideal for sustained deployment of sensitive electronic geophysical instruments. This means that the instruments themselves place a limitation on the research. A total of 6 borehole strainmeters have been deployed in Yellowstone since the expansion of the Earthscope Plate Boundary Observatory geodetic program. At the time of this research, only two of the six borehole strainmeters are recording data that is viable for use in constraining geophysical models. This limits the repeatability of this research, and limits the sources of data for future studies with these instruments.

7.5 Recommendations for further research

One of main concepts that this project and its predecessor [*Luttrell et al.*, 2013] propose is that strain is sensitive to shallow melt in the subsurface. Strain observed far from the lake is greater with melt in place than if there was no melt at all. Therefore, a future direction of this research would be to investigate if seiche related strain can be observed to the southeast of the lake, where there is no evidence of crystalizing magma beneath the surface. Currently, there are no borehole strain meters located in this area. However, there is a large network of GPS receivers in the Yellowstone region, including to the southeast of the lake. While including GPS receivers would increase the number of observation points, it is limited by scale. The strain we observe is on the order of nano-strain (ns), equivalent to 1 micron change in length over a kilometer. Typically, high resolution GPS receivers have an accuracy in the range of millimeters to centimeters.

It was observed in this project that seiching in Yellowstone Lake, and how it affects the surrounding crust, is more complex than currently accounted for. We observed influence of multiple seiche waves (~78, ~51, and ~25 minute periods) on borehole strainmeters in the region. Currently, records of lake level focus on capturing seiches with the ~78 minute period. To better characterize the dynamics of the various seiche waves present in Yellowstone Lake, it would be important to collect more

direct observations of lake level in the central basin and both the South and Southeast arms. By having a better understanding of dynamics of water movement in the lake, we can improve the understanding of its effect on the strain field in the caldera.

The available strain-field models are limited by the shape of the load, and the range of parameter space. Currently the model only accounts for the strain field produced by the ~78 minute period seiche load. From our results we determined that the loading in the lake and resultant deformation is more complex than a single period seiche can account for. Development of strain-field from model due to ~51 minute period seiche load shape could reconcile some of the discrepancies between the observed and modeled strain-field values that are noted in this paper.

There are several cases presented in this project where the observed values of seiche related strain provide no constraints on the available model space. The absent constraints on the subsurface with the strain-field models could be reconciled if the resolution of the model parameters was increased, and their range was broadened.

CHAPTER 8. CONCLUSIONS

The relationship between seiche waves in Yellowstone Lake and the strain response they induce in the caldera has the potential to provide insights into the Yellowstone magmatic system. Results indicate that for each strain component at each strainmeter the relationship between the seiche amplitude and strain response is self-consistent and follows a positive linear relationship even for strains less than ~1 ns. This demonstrates that this phenomena is not an isolated event.

Evaluation of the available two-layered viscoelastic model due to a seiche load with a ~78 minute period provides constraints of the structural and rheological properties of the shallow crust of the Yellowstone caldera. Constraints on the plate thickness (H) and Young's Modulus (E_1) suggest a laterally heterogeneous subsurface structure and rheology. Within the caldera the depth is greater in the southeast (under the lake) and shallows towards the northwest. Similarly, where magma is shallower the crust is weaker. This would occur if the local rock was substantially thermally weakened. This interpretation is consistent with seismic tomography studies that place low velocity zones (interpreted to be crystallizing magma) at depths >9 km beneath the southern portions of the caldera and shallowing out to 3km in the north [*Chu et al.*, 2010; *Husen et al.*, 2004]. Crustal deformation studies [*Chang et al.*, 2010; *Chang et al.*, 2007] and gravity observations [*DeNosaquo et al.*, 2009] also suggest a partially molten material at depths of 7-10 km. Temporal observations coupled with the constraints for the two-layered model constrain the viscosity (η) of the lower layer to $\leq 10^{11}$ and $\leq 10^{13}$ Pa s at B206 and B950 respectively. This which corresponds to a mush of 30 - 40% melt fraction. However, this fraction may vary depending on the volatile content of the melt.

The Yellowstone Volcanic field is an extensive and dynamic system that has shaped North America over its long history. The results presented in this research provide important insights into the structure and rheology beneath the caldera. These factors are important in the characterization of geologic hazard in the region.

REFERENCES

Ardia, P., D. Giordano, and M. W. Schmidt (2008), A model for the viscosity of rhyolite as a function of H2O-content and pressure: A calibration based on centrifuge piston cylinder experiments, *Geochimica et Cosmochimica Acta*, *72*(24), 6103-6123, doi:10.1016/j.gca.2008.08.025.

Chang, W. L., R. B. Smith, J. Farrell, and C. M. Puskas (2010), An extraordinary episode of Yellowstone caldera uplift, 2004-2010, from GPS and InSAR observations, *Geophysical Research Letters*, *37*, L23302-L23302, doi:10.1029/2010GL045451.

Chang, W. L., R. B. Smith, C. Wicks, J. M. Farrell, and C. M. Puskas (2007), Accelerated Uplift and Magmatic Intrusion of the Yellowstone Caldera, 2004 to 2006, *Science*, *318*, 952-956, doi:10.1126/science.1146842.

Christiansen, R. L., J. B. Lowenstern, R. B. Smith, H. Heasler, L. A. Morgan, M. Nathenson, L. G. Mastin, L. J. P. Muffler, and J. E. Robinson (2007), Preliminary Assessment of Volcanic and Hydrothermal Hazards in Yellowstone National Park and Vicinity, *Volcanoes: Formation, Eruptions and Modelling*, 94-94.

Chu, R., D. V. Helmberger, D. Sun, J. M. Jackson, and L. Zhu (2010), Mushy magma beneath Yellowstone, *Geophysical Research Letters*, *37*, L01306-L01306, doi:10.1029/2009GL041656.

DeNosaquo, K. R., R. B. Smith, and A. R. Lowry (2009), Density and lithospheric strength models of the Yellowstone-Snake River Plain volcanic system from gravity and heat flow data, *Journal of Volcanology and Geothermal Research*, *188*, 108-127, doi:10.1016/j.jvolgeores.2009.08.006.

Farrell, J., R. B. Smith, T. A. Taira, W. L. Chang, and C. M. Puskas (2010), Dynamics and rapid migration of the energetic 2008-2009 Yellowstone Lake earthquake swarm, *Geophysical Research Letters*, *37*, L19305-L19305, doi:10.1029/2010GL044605.

Gladwin, M. (1984), High-precision multicomponent borehole deformation monitoring, *Review of Scientific Instruments*, *55*(12), doi:10.1063/1.1137704.

Hildreth, W. (1981), Gradients in Silicic Magma Chambers: Implications for Lithospheric Magmatism, *Journal of Geophysical Research*, *86*(B11), 10153-10192, doi:10.1029/JB086iB11p10153.

Hildreth, W., A. N. Halliday, and R. L. Christiansen (1991), Isotopic and chemical evidence concerning the genesis and contomination of basaltic and throlitic magma beneath the yellowstone plateau volcanic field, *Journal of Petrology*, *32(1)*, 63-138, doi:10.1093/petrology/32.1.63.

Hodgkinson, K., J. Langbein, B. Henderson, D. Mencin, and A. Borsa (2013), Tidal calibration of plate boundary observatory borehole strainmeters, *Journal of Geophysical Research: Solid Earth*, *118*, 447-458, doi:10.1029/2012JB009651.

Husen, S., R. B. Smith, and G. P. Waite (2004), Evidence for gas and magmatic sources beneath the Yellowstone volcanic field from seismic tomographic imaging, *Journal of Volcanology and Geothermal Research*, *131*, 397-410, doi:10.1016/S0377-0273(03)00416-5.

Lehman, J. A., B. Smith, and M. Schilly (1982), Upper crustal structure of the Yellowstone caldera from seismic delay time analyses and gravity correlations, *Journal of Geophysical Research*, *87*(B4), 2713-2730.

Lowenstern, J. B., and S. Hurwitz (2008), Monitoring a supervolcano in repose: Heat and volatile flux at the Yellostone Caldera, *Elements*, *4*, 35-40, doi:10.2113/GSELEMENTS.4.1.35.

Lowenstern, J. B., R. B. Smith, and D. P. Hill (2006), Monitoring super-volcanoes: geophysical and geochemical signals at Yellowstone and other large caldera systems, *Philosophical transactions. Series A, Mathematical, physical, and engineering sciences*, *364*, 2055-2072, doi:10.1098/rsta.2006.1813.

Luttrell, K., D. Mencin, O. Francis, and S. Hurwitz (2013), Constraints on the upper crustal magma reservoir beneath Yellowstone Caldera inferred from lake-seiche induced strain observations, *Geophysical Research Letters*, *40*, 501-506, doi:10.1002/grl.50155.

Luttrell, K., and D. Sandwell (2010), Ocean loading effects on stress at near shore plate boundary fault systems, *Journal of Geophysical Research*, *115*, B08411-B08411, doi:10.1029/2009JB006541.

Luttrell, K., D. Sandwell, B. Smith-Konter, B. Bills, and Y. Bock (2007), Modulation of the earthquake cycle at the southern San Andreas fault by lake loading, *Journal of Geophysical Research*, *112*, B08411-B08411, doi:10.1029/2006JB004752.

Miller, S., and B. Smith (1999), P and S velocity structure of the Yellowstone volcanic field from local earthquake and controlled-source tomography, *Journal of Geophysical Research*, *104*(B7), 15,105-115,121.

Pelton, J. R., and R. B. Smith (1979), Recent crustal uplift in yellowstone national park, *Science*, *206*, 1179-1182.

Petford, N. (2003), Rheology of Granitic Magmas During Ascent and Emplacement, Annual Review of Earth and Planetary Sciences, 31, 399-427, doi:10.1146/annurev.genom.3.022502.103043.

Platzman, G. W., G. A. Curtis, K. S. Hansen, and R. D. Slater (1981), Normal Modes of the World Ocean. Part II: Description of Modes in the Period Range 8 to 80 Hours, *Journal of Physical Oceanography*, *11*, 579-603, doi:10.1175/1520-0485(1981)<0579:NMOTWO>2.0.C);2.

Rao, D. B. (1966), Free gravitational oscillations in rotating rectangular basins, *Journal of Fluid Mechanics*, *25*(3), 523-555, doi:10.1175/1520-0485(1981)<0579:NMOTWO>1.0.C);2.

Roeloffs, E. (2010), Tidal calibration of Plate Boundary Observatory borehole strainmeters: Roles of vertical and shear coupling, *Journal of Geophysical Research*, *115*, B06405-B06405, doi:10.1029/2009JB006407.

Seats, K. J., and J. F. Lawrence (2014), The seismic structure beneath the Yellowstone Volcano Field from ambient seismic noise, *Geophysical Research Letters*, *41*, 8277-8282, doi:10.1002/2014GL061913.

Smith, B., and D. Sandwell (2003), Coulomb stress accumulation along the San Andreas Fault system, *Journal of Geophysical Research*, *108*(B6), 2296-2296, doi:10.1029/2002jb002136.

Smith, B., and D. Sandwell (2004), A three-dimensional semianalytic viscoelastic model for time-dependent analyses of the earthquake cycle, *Journal of Geophysical Research*, *109*, B12401-B12401, doi:10.1029/2004JB003185.

Smith, R. B., and L. W. Braile (1994), The Yellowstone Hotspot, *Journal of Volcanology and Geothermal Research*, *61*, 121-187, doi:10.1016/0377-0273(94)90002-7.

Smith, R. B., M. Jordan, B. Steinberger, C. M. Puskas, J. Farrell, G. P. Waite, S. Husen, W. L. Chang, and R. O'Connell (2009), Geodynamics of the Yellowstone hotspot and mantle plume: Seismic and GPS imaging, kinematics, and mantle flow, *Journal of Volcanology and Geothermal Research*, *188*, 26-56, doi:10.1016/j.jvolgeores.2009.08.020.

Turcotte, D. L., and G. Schubert (2002), *Geodynamics*, 456 pp., Cambridge University Press.

Vazquez, J. A., S. F. Kyriazis, M. R. Reid, R. C. Sehler, and F. C. Ramos (2009), Thermochemical evolution of young rhyolites at Yellowstone: Evidence for a cooling but periodically replenished postcaldera magma reservoir, *Journal of Volcanology and Geothermal Research*, *188*, 186-196, doi:10.1016/j.jvolgerores.2008.11.030.

Waite, G. P., and R. B. Smith (2002), Seismic evidence for fluid migration accompanying subsidence of the Yellowstone caldera, *Journal of Geophysical Research*, *107*(B9), 2177-2177, doi:10.1029/2001JB000586.

Wicks, C. W., W. Thatcher, D. Dzurisin, and J. Svarc (2006), Uplift, thermal unrest and magma intrusion at Yellowstone caldera, *Nature*, *440*, 72-75, doi:10.1038/nature04507.

APPENDIX

A.1 Extended description of pilot study

In order to apply these ideas of the seiche-strain relationship, *Luttrell et al.* [2013] set out about developing methods to utilize this unique system to constrain properties of the subsurface beneath Yellowstone caldera. This process could be divided into three distinct steps. First, was to develop a model of seiche waves within Yellowstone Lake based on bathymetry of the basin that agreed with observations of the seiches measured on APGs deployed in the lake. Second, was to analyze seiche related deformation in the caldera measured on the borehole strainmeters available. The final step involved the evaluation of modeled 3-D strain fields due to the water mass movement in the lake utilizing numerical models of varying structure and rheologies.

The first step involved the formulation of lake models that could accurately represent the normal modes of Yellowstone Lake that have been observed on deployed APGs. Using observations of the lake bathymetry, these normal modes were calculated by way of Proudman's method [*Platzman et al.*, 1981; *Rao*, 1966]. Through this lake modeling it was determined that the 78 minute period seiche corresponded to the longest natural period of the lake basin, which was equivalent to water mass movement from the West Thumb basin to the Southeast Arm. Additionally, a secondary mode of water mass movement between the Southeast Arm and the Central Basin was determined and corresponds to the observed seiche with a ~51 minute period . By combining the models of the shape of the lake load, with direct observations seiches in the lake measured on absolute pressure gauges, it would be possible to represent the changes in Yellowstone Lake through time.

The next step the authors of *Luttrell et al*., [2013] was to analyze the seiche related crustal strain signals as observed on the borehole strainmeters installed in the caldera. Before data from borehole strainmeters can be used in geophysical modeling, you must first go through the arduous process of "calibrating" the borehole strainmeter instrument observations (measured on four extensometers within the strainmeter housing). This calibration converts measurements from three (or four) of the instruments extensometers to the three horizontal components of the strain tensor: areal strain(ε_A), differential strain(ε_D), and engineering shear strain(ε_S) [*Hodgkinson et al.*, 2013; *Roeloffs*, 2010]. It was after this extensive process that the time series data could be analyzed and peak-to-trough amplitudes of the seiche related strain transients could be determined based on the unique periodic nature that connects the two phenomena.

With the seiche-strain observations, the next step was to develop a way on which to use these observations to infer (derive) properties of the subsurface beneath Yellowstone caldera. This was accomplished by using numerical models of different structure and rheology to generate a 3-D strain field due to a given seiche load. Two models were considered by *Luttrell et al*. [2013] for potential subsurface compositions. The first model, puts the depth of compensation (the depth that below which the seiche loading does not affect) within the shallow solid crust, represented by an elastic half-space. Their second model, places the depth of compensation within a body of magma present in the shallow crust, represented by a layered model of an elastic layer overlying a viscoelastic half-space. The modeled strain field was generated by convolving the 2-D shape of the seiche load with the models varying over their parameter space which considers varying properties of the subsurface, in particular the depth of compensation (H), Young's modulus (*E1*), Poisson's Ratio (v1), and the ratio of shear moduli between the elastic and viscoelastic layers(μ_1/μ_2).

The most notable limitation of previous research for the proposed methods was the lack of available time series data of lake level observations. During the initial deployments of APG instruments only 20 weeks of data were collected. From these 20 weeks of data only one high-amplitude seiche event was recorded. All subsequent analysis was dependent on this single observed seiche event. Therefore

as a part of this proposed research, there will be continued deployment of campaign APG instruments in an effort to capture additional measurements of high-amplitude seiche events. The analysis will be repeated with the greater number of events to make previous findings more robust, and determine the possible range of crustal strains due to varying seiche loads

All direct observations of seiche amplitude within Yellowstone Lake were measured at a single location, Grant Boat Dock in West Thumb basin. Therefore, the shape of the ~78 minute period lake seiche in the basin depended upon hydrodynamic modeling of the Yellowstone Lake basin. This modeled load was used in the modeling of crustal deformation. Direct observations of lake level perturbations at additional locations within the Yellowstone lake basin will aid in determining the accuracy of the hydrodynamic modeling, and therefore the confidence in using the established load shape in evaluating modeled seiche associated crustal strain. The deployment of instruments in additional locations in the basin will also provide observational data of higher order seiches (e.g. ~51 minutes, ~35 minutes) that are present within Yellowstone Lake, some of which may not be observable on APGs deployed in the West Thumb basin.

Only observations associated with the dominant seiching mode of ~78 minutes were utilized for evaluating the models. Lake basin models show that the ~78 minute period signal is consistent with water mass transfer between the West Thumb basin and the Southeast Arm. However, Yellowstone Lake is an irregular shaped basin and can be considered composed of several smaller partially enclosed basins, each with their own, albeit shorter period and smaller amplitude, seiche waves. These additional shorter period seiches present in Yellowstone Lake could be contained to the West Thumb basin itself, the central basin to the South and Southeast Arms, the central basin to the West Thumb basin, and the Arms themselves. Therefore, it would be beneficial to take measurements in the lake in these separate sub basins to better characterize and understand the dynamics of the seiche loading. Eventually this would entail using crustal strain observations to evaluate strain-field models due to the shorter period seiches.

Conclusions from previous research were based on observations of seiche related deformation from only one (B206) of the five borehole strainmeters presently recording in the Yellowstone caldera. The primary reason for this was that of the five instruments installed in 2008, only three proved fully successful. B205, B206, and B944 all provided sufficiently clean and artifact free data that could be calibrated and utilized for geophysical modeling. B205 would later be decommissioned due to environmental conditions in 2010, before the time period when the previous research was conducted. Only observations from calibrated data from B206 and B944 were available for use in analysis. However, as of 2013, another borehole strainmeter (B950) has been installed near the original location of B205. Data from B207 and B208 was not utilized previously because the time series recorded proved too noisy to determine absolute amplitude of seiche associated strain. However, the quality and clarity of the data at these locations may have improved since the conclusion of the pilot study, therefore they will re-assessed for their potential to give measurements of the seiche associated strain field. It is also possible to investigate alternative ways to approximate the seiche associated strain amplitude in the time series data, which will aid in using time series data where the amplitudes are relatively small. It is important to utilize as many possible observations of the strain field in the caldera to improve the estimates of the magma depth and melt fraction. This is also because prior modeling of the seiche associated strain field shows that the loading is unevenly distributed (the shape of the lake), and that the magnitude of deformation varies depending on the distance and the azimuth in relation to the lake.

A.2 Time series processing and uncertainties

A potential area of concern in the analysis of time series data is the extent that varying degrees of filtering may affect the confidence we place on the measurements take. We suggest that for the purposes of this study, the degrees of filtering used will not significantly affect our measurements. To determine this we tested the filtering type used in the signal processing of this study with respect to the

target 78 minute period seiche wave measured on the absolute pressure gauge at GBD. The filter utilized is a bandpass-type filter. The filter was applied to segments of the time series data that had been de-trended by removing the line of best fit from the data. The high pass portion of the filter was measured in days, and the low pass portion was measured in minutes. To test the effect of varying degrees of filtering has on measurements taken, we ran a select window of time (that would equate to the duration of a regular seiche wave) through a bandpass filter repeatedly with varying high and low pass values. We varied the high pass (Tcd) from 1 to 0.1 day(s) in steps of 0.1 days, and the low pass (Tcm) from 5 to 40 minutes in steps of 5 minutes. The effects of varying filtering parameters were examined by comparing cases where both Tcd and Tcm vary, variable Tcd with constant Tcm, and varying Tcm with Tcd constant. Measured points on the time series were taken from maximum and minimum values of the peaks and troughs for each combination of Tcd and Tcm. These peak and trough pairs were measured because they are the points picked for determining the amplitude of a measured seiche wave and associated strain response. The mean and standard deviation were calculated at each sample point with all the measured values determined by the values of Tcd and Tcm.

We find that with the applied filters and varying degrees of Tcd and Tcm, where changes in the Tcd have a greater effect on the measured values than variations in Tcm. This effect is more pronounced sections of the time series. However, these results could also be attributed to an edge effect of the high pass portion of the filter and the edge of the windowed time series. With that in mind, we found it optimal to choose an appropriate high pass cut off value, and vary the low pass cut off as needed (so as to not remove the desired signals) for the selection of peak-to-trough amplitude of seiche waves and their associated strain response. When this was done (with a Tcd of 0.3 days) we found that the percent change in the mean for a peak or trough sample point ranges from 5 to 10 % with an average across the whole time series selection of 5.4%. Therefore from this we concluded that the methods of bandpass filtering are suitable for use in this study and will not greatly affect measurements with varying the degrees of filtering (as long as it is kept to appropriate levels).

A.3 Extended description of processing and calibration of borehole strainmeter data

The gauges of borehole strainmeters record the linear elongation along the axis of the gauge, which can be converted to linear strain by dividing by the instruments diameter. However, this linear strain is not the same as the formation strain because the strainmeter itself and the grout holding it in place have different elastic moduli from the surrounding formation [*Roeloffs*, 2010]. Therefore, it is necessary to "calibrate" borehole strainmeter data before incorporating it into geophysical models that represent tectonic or volcanic processes. The end result of calibration of borehole strainmeter data is to give the formation strain as if the strainmeter was not in place. The process of calibration starts with the approximation of a "coupling matrix" that expresses the linear strain from the borehole strainmeter outputs as combinations of the formation strain. This method assumes that the formation strain can be approximated as linear combinations of the strainmeter outputs. After a coupling matrix has been estimated, it is inversed to generate a "calibration matrix" which expresses the horizontal strain components areal strain (ε_A), differential strain (ε_D), and engineering shear strain (ε_S) as combinations of the borehole strainmeter gauge outputs [*Hodgkinson et al.*, 2013; *Roeloffs*, 2010]. For this project we will utilize the calibration of borehole strainmeter data by using modeled Earth tides. When using modeled each tides as a reference signal the procedure to produce a coupling matrix involves comparing the estimated components of earth tides recorded on each gauge[*Hodgkinson et al.*, 2013].

Table A.1 Estimated earth tide components for calibration of borehole strainmeter data

Strainmeter	*Gauge*	M_2		O_1	
		Amplitude	*Phase*	*Amplitude*	*Phase*
B944	e1	22.62	11.39	9.09	-6.64
	e2	9.72	-167.62	3.96	177.62
	e3	1.21	-54.32	1.17	-174.82
	e4	16.26	6.53	5.76	-6.17
B208	e1	8.41	120.22	8.21	-23.16
	e2	8.55	-82.06	0.93	76.51
	e3	18.47	18.95	5.92	-3.11
	e4	13.36	71.28	6.82	-20.43
B206	e1	12.55	8.332	2.91	4.69
	e2	13.104	18.727	9.76	-21.15
	e3	9.426	-143.576	3.13	68.71
	e4	3.749	-98.111	3.70	106.52
B950	e1	11.44	3.113	1.581	131.716
	e2	10.943	80.00	6.191	60.598
	e3	13.262	-134.574	3.788	71.751
	e4	9.499	-81.752-	4.793	89.638

Table A.2: Theoretical earth tide components for calibration of borehole strainmeter data

Strainmeter	*Strain Component*	M_2		O_1	
		Amplitude	*Phase*	*Amplitude*	*Phase*
B944	ε_A	13.08	3.13	11.51	3.87
	ε_D	8.01	-169.97	2.21	-12.73
	ε_S	7.54	-102.49	3.37	82.35
B208	ε_A	13.00	3.19	11.51	3.82
	ε_D	8.05	-169.83	2.21	-12.81
	ε_S	7.58	-102.20	3.36	82.42
B206	ε_A	12.90	3.37	11.51	3.83
	ε_D	8.03	-169.63	2.20	-12.97
	ε_S	7.62	-101.99	3.35	82.37
B950	ε_A	12.8922	3.27	11.5155	3.87
	ε_D	7.9878	-169.57	2.2016	-13.01
	ε_S	7.6194	102.20	3.3466	82.36

Table A.3: Atmospheric pressure response coefficients

Strainmeter	*e1*	*e2*	*e3*	*e4*
[1]B944	-12.2	-3.3	-5.7	-10.5
[1]B208	-6.60	-4.2	-7.4	-8.1

(Table A.3 continued)

Strainmeter	*e1*	*e2*	*e3*	*e4*
[2]B950	-5.7	-4.8	-5.4	-6.0
[2]B206	-4.2	-2.4	-4.9	-5.4

[1] from *Hodgkinson et al.* [2013]

[2] from UNAVCO ftp

Table A.4 Calibration matrices

Strainmeter	*Calibration matrix*				*Strainmeter*	*Calibration matrix*			
[1]B944	-4.819	0.575	-8.792	8.118	[2]B208	0.8404	1.272	0.902	-0.093
	-2.845	0.319	-5.908	3.837		0.5846	0.366	-0.310	-0.086
	-7.061	1.511	-6.825	10.756		0.3007	0.760	0.043	-0.374
[1]B206	0.456	1.052	0.689	0.314	[2]B950	1.451	3.651	1.531	2.685
	-0.632	0.329	0.524	-0.295		-0.379	0.391	0.474	0.095
	0.444	-0.082	0.690	0.792		0.099	0.034	0.371	0.458

[1] from *Hodgkinson et al.* [2013]

[2] calculated using equation A.1

A.4 Extended data tables

Table A.5 Lake pressure gauge data logs

Log Date Start	*Log Date End*	*Sample Rate (s)*	*Site Name*	*Latitude*	*Longitude*
8/8/2011	8/29/2011	60	Grant Boat Dock	44.391827°N	-110.54881°W
9/13/2011	10/4/2011	60			
11/18/2011	1/26/2012	60			
6/26/2012	7/29/2012	60			
8/18/2014	1/3/2015	120			
2/8/2015	4/18/2015	60			
6/26/2015	9/14/2015	60			
9/14/2015	11/22/2015	60			
5/20/2016	7/11/2016	60			
7/11/2016	9/15/2016	60			
8/18/2014	1/3/2015	120	Pumice Point North	44.452614°N	-110.50091°W
2/8/2015	4/18/2015	60			
6/26/2015	9/14/2015	60			
8/18/2014	1/3/2015	120	Sand Point North	44.498753°N	-110.41882°W
2/8/2015	4/18/2015	60			
6/26/2015	9/14/2015	60			
6/8/2016	7/9/2016	60	Holmes Point	44.537384°N	-110.29530°W
7/10/2016	9/15/2016	60	North Fir Turnout	44.46915°N	-110.45846°W

Table A.6 Full list of measured seiche waves in Yellowstone Lake

		GBD		PPN		SPN	
Onset	*End*	*Date Max.*	*Amp.*	*Date Max.*	*Amp.*	*Date Max.*	*Amp.*
Date/Time	*Date/Time*	*Amp.*	*(cm)*	*Amp.-*	*(cm)*	*Amp.*	*(cm)*
8/25/11 2:00	8/26/11 20:00	8/25/11 13:18	7.1	--	--	--	--
7/12/12 1:00	7/13/12 16:00	7/12/12 9:09	8.3	--	--	--	--
8/20/14 3:30	8/21/14 0:00	8/20/14 9:00	2.7	8/20/14 14:09	2.1	8/20/14 2:23	1.8
8/22/14 2:00	8/23/14 7:00	8/22/14 8:32	3.9	8/22/14 7:43	3.7	8/22/14 6:57	2.1
8/25/14 21:00	8/27/14 9:00	8/26/14 0:40	1.8	8/25/14 22:31	3.7	8/26/14 0:47	1
8/29/14 9:00	8/30/14 9:00	8/29/14 11:12	5.4	8/29/14 8:35	4.4	8/29/14 8:53	3.4
8/30/14 12:00	8/31/14 12:00	8/30/14 21:44	4.5	8/31/14 0:23	8.2	8/30/14 23:57	4.1
8/31/14 23:30	9/2/14 1:30	9/1/14 9:24	1.9	9/1/14 0:27	6.6	--	--
9/9/14 21:00	9/11/14 0:00	9/10/14 2:20	4.9	9/10/14 2:23	4.5	9/10/14 0:25	3.5
9/18/14 12:00	9/19/14 0:00	9/18/14 15:50	6.3	9/18/14 14:27	4.9	9/18/14 15:25	1.9
9/19/14 1:00	9/20/14 23:30	9/19/14 4:28	6.1	9/19/14 4:39	10.2	9/19/14 5:35	2
9/22/14 5:00	9/24/14 0:00	9/23/14 2:14	1.9	--	--	9/22/14 0:09	0.7
9/27/14 6:00	9/29/14 1:00	9/27/14 9:44	9.5	9/27/14 9:45	7.2	9/27/14 11:17	2.9
10/12/14 0:00	10/14/14 3:00	10/12/14 7:22	5.1	10/12/14 7:09	3.6	10/12/14 6:49	2.6
10/15/14 3:00	10/18/14 12:00	10/16/14 18:00	2.9	10/16/14 3:49	11.2	10/16/14 3:05	2.4
10/22/14 0:00	10/23/14 0:00	10/22/14 7:22	3.0	10/22/14 19:59	9.5	10/22/14 2:47	1.5
10/26/14 0:00	10/28/14 12:00	10/26/14 8:40	7.5	10/27/14 13:19	5.5	10/26/14 9:19	2.2
10/28/14 18:00	10/30/14 12:00	10/29/14 11:30	2.5	--	--	10/29/14 9:35	2.2
11/1/14 12:00	11/6/14 0:00	11/2/14 4:44	8.0	11/7/14 9:51	4.8	11/2/14 1:37	4.3
11/7/14 9:00	11/8/14 12:00	11/7/14 17:50	3.6	11/7/14 9:51	7.5	11/7/14 17:31	3
11/14/14 15:00	11/17/14 12:00	11/15/14 5:52	3.2	11/15/14 8:27	2.8	11/15/14 7:59	3.1
11/18/14 0:00	11/22/14 0:00	11/19/14 19:38	2.7	11/19/14 13:07	3.5	11/20/14 15:43	2.6
11/22/14 21:00	11/24/14 5:00	11/23/14 23:06	4.8	11/22/14 15:39	7	11/24/14 6:15	3
11/28/14 6:00	11/29/14 9:00	11/28/14 16:46	5.1	11/28/14 13:43	5.6	--	--
11/29/14 9:00	11/30/14 0:00	11/29/14 15:54	5.4	11/29/14 18:21	8.1	--	--
12/1/14 18:00	12/7/14 18:00	12/5/14 20:14	5.3	12/6/14 0:35	2.3	12/6/14 10:11	2.8
12/8/14 6:00	12/16/14 0:00	12/12/14 17:00	4.7	12/13/14 13:51	1.6	12/10/14 23:25	2.2
12/16/14 0:00	12/17/14 2:00	12/16/14 10:10	2.1	12/16/14 19:09	6.2	12/16/14 12:09	1.8
12/18/14 15:00	12/20/14 9:00	12/18/14 23:52	2.7	12/18/14 14:57	19.5	--	--
12/21/14 19:32	12/25/14 0:00	12/22/14 4:50	7.6	12/22/14 22:09	17.3	12/25/14 0:01	1.9
12/27/14 15:00	12/28/14 22:00	12/27/14 23:26	2.9	12/27/14 9:03	30.7	--	--
1/2/15 18:00	1/3/15 15:10	1/3/15 1:00	3.0	1/3/15 11:35	4.1	1/2/15 18:01	1.6
2/10/15 0:00	2/15/15 0:00	2/10/15 6:09	2.9	2/11/15 19:45	10.3	2/9/15 20:26	2
2/16/15 6:00	2/18/15 0:00	2/17/15 8:10	1.8	2/16/15 21:51	2.2	2/17/15 7:37	0.7
2/19/15 0:00	2/20/15 3:00	2/19/15 12:36	1.6	--	--	2/19/15 11:15	0.9
2/21/15 0:00	2/25/15 1:00	2/22/15 10:45	1.8	2/22/15 10:42	1.5	2/24/15 20:17	1.2
2/25/15 21:00	3/8/15 3:00	2/27/15 18:12	3.1	2/27/15 15:33	3.1	2/27/15 22:45	0.7
3/8/15 9:00	3/9/15 3:00	3/8/15 14:39	1.5	--	--	--	--
3/10/15 0:00	3/13/15 15:00	3/12/15 5:03	3.5	3/12/15 11:15	7	--	--
3/14/15 6:00	3/17/15 0:00	3/15/15 14:34	7.3	3/15/15 5:10	10.4	3/16/15 4:31	1.9

(Table A.6 continued)

		GBD		PPN		SPN	
Onset Date/Time	*End Date/Time*	*Date Max. Amp.*	*Amp. (cm)*	*Date Max. Amp.-*	*Amp. (cm)*	*Date Max. Amp.*	*Amp. (cm)*
3/28/15 18:00	3/29/15 6:00	3/29/15 2:00	4.9	--	--	--	--
4/4/15 0:00	4/6/15 0:00	4/5/15 11:09	2.4	4/4/15 22:17	10.1	--	--
4/6/15 12:00	4/9/15 3:00	4/7/15 14:29	4.7	4/9/15 0:09	8.1	--	--
4/10/15 0:00	4/14/15 12:00	4/12/15 20:58	2.4	4/11/15 18:04	11.7	--	--
4/15/15 12:00	4/17/15 0:00	4/15/15 14:49	3.1	4/15/15 21:58	19.1	--	--
6/28/15 9:00	6/28/15 0:00	6/28/15 12:05	1.5	--	--	--	--
6/29/15 0:00	6/30/15 0:00	6/29/15 5:12	2.9	--	--	--	--
7/6/15 6:00	7/6/15 12:00	7/6/15 8:31	5.5	--	--	7/6/15 11:18	3.4
7/14/15 0:00	7/14/15 15:00	7/14/15 9:23	3.1	--	--	7/14/15 13:02	3.6
7/14/15 18:00	7/15/15 3:00	7/14/15 21:13	2.4	--	--	--	--
7/17/15 0:00	7/18/15 12:00	7/17/15 3:58	3.2	--	--	--	--
7/21/15 6:00	7/21/15 18:00	7/21/15 12:58	1.7	--	--	--	--
7/22/15 0:00	7/22/15 23:00	7/22/15 13:15	1.9	--	--	7/22/15 23:08	1.5
7/23/15 0:00	7/23/15 17:00	7/23/15 8:59	3.0	--	--	7/23/15 21:11	1.7
7/28/15 0:00	7/29/15 23:30	7/28/15 6:12	6.7	--	--	--	--
8/4/15 0:00	8/5/15 0:00	8/4/15 5:00	3.6	--	--	8/4/15 21:43	2
8/5/15 0:00	8/6/15 12:00	8/5/15 22:04	7.1	--	--	8/5/15 18:48	2.7
8/8/15 12:00	8/9/15 15:00	8/9/15 2:20	1.9	--	--	8/8/15 20:26	1.9
8/26/15 12:00	8/27/15 12:00	8/27/15 4:32	2.7	--	--	8/27/15 2:08	3.5
8/29/15 18:00	8/30/15 6:00	8/30/15 1:00	2.5	--	--	--	--
8/30/15 6:00	8/30/15 12:00	8/30/15 8:43	6.7	--	--	8/30/15 18:12	5.3
9/3/15 0:00	9/3/15 20:00	9/3/15 14:50	5.2	--	--	9/3/15 18:36	4.9
10/30/15 0:00	11/2/15 0:00	10/31/15 0:24	7.4	--	--	--	--
11/2/15 0:00	11/6/15 0:00	11/3/15 19:00	6.4	--	--	--	--
5/21/16 14:00	5/22/16 17:00	5/22/15 3:46	8.2	--	--	--	--
6/14/16 0:00	6/20/16 0:00	6/14/16 18:51	5.9	--	--	--	--
6/28/16 22:45	7/2/16 0:00	6/29/16 0:25	10.5	--	--	--	--
7/13/16 0:00	7/14/16 9:00	7/13/16 3:43	5.5	--	--	--	--
8/15/16 0:00	8/16/16 15:00	8/15/16 4:02	7.4	--	--	--	--
8/24/16 21:00	8/26/16 3:00	8/24/16 23:10	6.1	--	--	--	--
9/4/16 0:00	9/7/16 0:00	9/5/16 10:00	7.8	--	--	--	--

Table A.7 Estimated amplitude of seiche waves–APGs

Seiche Event Window	*APG*	*78 minute component*		*51 minute component*		*25 minute component*	
		Lake Height (cm)	*RMSE*	*Lake Height (cm)*	*RMSE*	*Lake Height (cm)*	*RMSE*
26 August 2011 3:00 – 7:00	GBD	3.8	0.18	0.1	1.35	0.1	1.34
	PPN	--[2]	--[2]	--[2]	--[2]	--[2]	--[2]
	SPN	--[2]	--[2]	--[2]	--[2]	--[2]	--[2]

(Table A.7 continued)

Seiche Event Window	*APG*	*78 minute component*		*51 minute component*		*25 minute component*	
		Lake Height (cm)	*RMSE*	*Lake Height (cm)*	*RMSE*	*Lake Height (cm)*	*RMSE*
12 July 2012	GBD	8.2	0.66	0.5	2.98	0.6	3.00
9:00 – 13:00	PPN	--[2]	--[2]	--[2]	--[2]	--[2]	--[2]
	SPN	--[2]	--[2]	--[2]	--[2]	--[2]	--[2]
27 September 2014	GBD	8.2	0.16	1.1	2.92	0.3	2.94
10:30 – 14:30	PPN	3.3	0.30	0.1	2.37	--[1]	--[1]
	SPN	0.1	0.90	1.1	0.47	0.1	0.88
27 October 2014	GBD	5.4	0.15	0.3	1.92	--[1]	--[1]
8:00 12:00	PPN	1.8	0.75	0.1	1.47	0.3	1.46
	SPN	0.3	0.26	0.3	0.23	--[1]	--[1]
2 November 2014	GBD	4.9	0.15	1.2	1.77	0.1	1.79
10:00- 14:00	PPN	1.5	1.79	0.6	2.04	0.4	2.09
	SPN	0.2	0.87	1.1	0.36	0.1	0.88
22 December 2014	GBD	4.9	0.38	0.1	1.79	--[1]	--[1]
8:00 – 12:00	PPN	1.5	0.79	0.2	1.31	--[1]	--[1]
	SPN	0.2	0.48	0.3	0.46	0.3	0.46
15 March 2015	GBD	6.4	0.35	1.1	2.25	0.12	2.28
13:00 – 17:00	PPN	1.4	0.20	0.1	0.41	0.1	1.08
	SPN	0.3	0.37	0.5	0.19	--[1]	--[1]
5 August 2015	GBD	4.2	0.25	0.1	1.5	0.14	1.5
8:00 – 12:00	PPN	--[2]	--[2]	--[2]	--[2]	--[2]	--[2]
	SPN	--[2]	--[2]	--[2]	--[2]	--[2]	--[2]
31 October 2015	GBD	3.6	0.49	0.1	1.36	0.49	1.35
8:00 – 12:00	PPN	--[2]	--[2]	--[2]	--[2]	--[2]	--[2]
	SPN	--[2]	--[2]	--[2]	--[2]	--[2]	--[2]
22 May 2016	GBD	5.6	0.30	0.7	2.02	0.1	2.04
6:00 – 10:00	PPN	--[2]	--[2]	--[2]	--[2]	--[2]	--[2]
	SPN	--[2]	--[2]	--[2]	--[2]	--[2]	--[2]
29 June 2016	GBD	7.3	2.6	0.7	2.61	0.2	2.65
6:00 – 10:00	PPN	--[2]	--[2]	--[2]	--[2]	--[2]	--[2]
	SPN	--[2]	--[2]	--[2]	--[2]	--[2]	--[2]
15 August 2016	GBD	4.7	0.19	--[1]	--[1]	0.2	1.67
9:00 – 13:00	PPN	--[2]	--[2]	--[2]	--[2]	--[2]	--[2]
	SPN	--[2]	--[2]	--[2]	--[2]	--[2]	--[2]
5 September 2016	GBD	6.0	0.25	1.0	2.17	0.2	2.21
13:30 – 18:30	PPN	--[2]	--[2]	--[2]	--[2]	--[2]	--[2]
	SPN	--[2]	--[2]	--[2]	--[2]	--[2]	--[2]

[1] No time series data available

[2] Measured value is negligible

Table A.8 Estimated strain amplitude for ~78 minute period seiche–BSM

Seiche Event Window	*Strain*	*B944*		*B208*		*B206*		*B950*	
		Amp. (ns)	*RMSE*	*Amp. (ns)*	*RMSE*	*Amp. (ns)*	*RMSE*	*Amp. (ns)*	*RMSE*
26 August 2011	ε_A	7.17	3.66	--[2]	--[2]	1.19	0.97	--[1]	--[1]
3:00 – 7:00	ε_D	5.55	4.52	--[2]	--[2]	0.49	0.35	--[1]	--[1]
	ε_S	15.83	2.78	--[2]	--[2]	1.21	0.67	--[1]	--[1]
12 July 2012	ε_A	18.00	4.27	--[2]	--[2]	3.65	1.09	--[1]	--[1]
9:00 – 13:00	ε_D	16.34	3.66	--[2]	--[2]	1.13	0.30	--[1]	--[1]
	ε_S	43.46	4.52	--[2]	--[2]	2.16	0.99	--[1]	--[1]
27 September 2014	ε_A	12.39	2.28	2.46	2.09	--[2]	--[2]	8.06	10.86
10:30 – 14:30	ε_D	9.05	2.44	0.21	0.47	--[2]	--[2]	0.69	0.81
	ε_S	32.36	1.60	2.09	0.51	--[2]	--[2]	1.21	1.34
27 October 2014	ε_A	9.28	2.27	1.48	1.00	--[2]	--[2]	4.17	2.92
8:00 12:00	ε_D	9.05	2.44	0.42	0.22	--[2]	--[2]	0.14	0.18
	ε_S	21.54	1.03	1.12	0.26	--[2]	--[2]	0.37	0.33
2 November 2014	ε_A	9.98	3.48	4.40	2.16	--[2]	--[2]	8.9	7.21
10:00- 14:00	ε_D	8.51	2.57	0.93	1.00	--[2]	--[2]	0.64	0.36
	ε_S	22.45	4.25	1.96	0.85	--[2]	--[2]	1.10	0.78
22 December 2014	ε_A	9.05	1.71	3.21	0.80	--[2]	--[2]	2.56	5.38
8:00 – 12:00	ε_D	6.27	2.02	0.17	0.20	--[2]	--[2]	0.4	0.50
	ε_S	18.42	1.20	1.08	0.37	--[2]	--[2]	0.09	0.62
15 March 2015	ε_A	6.94	1.86	1.10	1.23	--[2]	--[2]	11.87	5.21
13:00 – 17:00	ε_D	5.21	2.27	0.49	0.27	--[2]	--[2]	0.71	0.39
	ε_S	21.74	0.78	1.06	0.40	--[2]	--[2]	1.11	0.59
5 August 2015	ε_A	6.69	1.54	0.23	1.58	--[2]	--[2]	4.06	6.48
8:00 – 12:00	ε_D	5.25	1.94	0.33	0.33	--[2]	--[2]	0.28	0.49
	ε_S	15.84	0.62	0.47	0.46	--[2]	--[2]	0.46	0.74
31 October 2015	ε_A	6.87	1.63	2.27	1.43	--[2]	--[2]	5.21	7.13
8:00 – 12:00	ε_D	6.54	1.79	0.11	0.26	--[2]	--[2]	0.18	0.46
	ε_S	13.26	0.77	0.59	0.32	--[2]	--[2]	0.56	0.86
22 May 2016	ε_A	9.85	1.80	1.91	1.45	--[2]	--[2]	4.40	6.68
6:00 – 10:00	ε_D	8.03	2.37	0.31	0.25	--[2]	--[2]	0.35	0.52
	ε_S	23.18	0.90	0.97	0.44	--[2]	--[2]	0.44	0.84
29 June 2016	ε_A	13.69	1.22	2.29	0.64	--[2]	--[2]	6.49	2.47
6:00 – 10:00	ε_D	11.56	0.98	0.16	0.20	--[2]	--[2]	0.51	0.19
	ε_S	31.41	1.61	1.32	0.16	--[2]	--[2]	0.67	0.27
15 August 2016	ε_A	5.49	1.24	1.16	0.62	--[2]	--[2]	2.85	3.25
9:00 – 13:00	ε_D	4.07	1.20	0.28	0.15	--[2]	--[2]	0.23	0.25
	ε_S	16.82	1.10	0.94	0.17	--[2]	--[2]	0.28	0.36
5 September 2016	ε_A	9.26	1.92	0.39	1.59	--[2]	--[2]	5.32	2.79
13:30 – 18:30	ε_D	7.71	2.13	0.11	0.23	--[2]	--[2]	0.42	0.22
	ε_S	22.82	1.09	0.90	0.70	--[2]	--[2]	0.52	0.29

[1] Time series data unavailable
[2] Data is unsuitable for use

Table A.9 Estimated amplitude of ~51 minute period seiche–BSM

Seiche Event Window	*Strain*	*B944*		*B208*		*B206*		*B950*	
		Amp. (ns)	*RMSE*	*Amp. (ns)*	*RMSE*	*Amp. (ns)*	*RMSE*	*Amp. (ns)*	*RMSE*
26 August 2011	ε_A	0.58	4.47	--[2]	--[2]	0.62	1.06	--[1]	--[1]
3:00 – 7:00	ε_D	1.16	4.93	--[2]	--[2]	0.18	0.4	--[1]	--[1]
	ε_S	0.63	6.28	--[2]	--[2]	0.51	0.8	--[1]	--[1]
12 July 2012	ε_A	1	7.71	--[2]	--[2]	0.43	1.71	--[1]	--[1]
9:00 – 13:00	ε_D	1.39	6.92	--[2]	--[2]	0.21	0.49	--[1]	--[1]
	ε_S	1.52	16.22	--[2]	--[2]	0.46	1.25	--[1]	--[1]
27 September 2014	ε_A	0.82	4.7	3.09	2.29	--[2]	--[2]	6.3	6.23
10:30 – 14:30	ε_D	0.55	4.71	1.25	0.56	--[2]	--[2]	0.19	0.48
	ε_S	3.49	11.52	0.25	0.89	--[2]	--[2]	0.63	0.82
27 October 2014	ε_A	0.44	4.02	1.01	1.13	--[2]	--[2]	1.14	2.6
8:00 12:00	ε_D	0.57	4.02	0.55	0.27	--[2]	--[2]	0.07	0.13
	ε_S	1.52	7.7	0.34	0.48	--[2]	--[2]	0.14	0.29
2 November 2014	ε_A	3.36	5.02	3.84	2.66	--[2]	--[2]	7.8	5.76
10:00- 14:00	ε_D	4.42	4.03	1.44	1.05	--[2]	--[2]	0.42	0.36
	ε_S	3.48	9.18	0.32	1.1	--[2]	--[2]	0.79	0.63
22 December 2014	ε_A	1.04	3.65	1.31	1.4	--[2]	--[2]	4.37	3.66
8:00 – 12:00	ε_D	0.78	3.04	0.17	0.22	--[2]	--[2]	0.41	0.36
	ε_S	0.47	6.69	0.49	0.55	--[2]	--[2]	0.56	0.38
15 March 2015	ε_A	4.55	3.1	2.25	1.31	--[2]	--[2]	6.07	5.1
13:00 – 17:00	ε_D	5.59	2.94	1.37	0.32	--[2]	--[2]	0.66	0.36
	ε_S	4.82	7.68	0.68	0.55	--[2]	--[2]	0.67	0.51
5 August 2015	ε_A	1.91	2.9	0.88	1.77	--[2]	--[2]	2.81	3.4
8:00 – 12:00	ε_D	2.42	2.77	0.38	0.38	--[2]	--[2]	0.26	0.26
	ε_S	0.63	5.66	0.26	0.51	--[2]	--[2]	0.43	0.36
31 October 2015	ε_A	3.49	2.93	1.79	1.65	--[2]	--[2]	5.1	5.26
8:00 – 12:00	ε_D	3.79	2.93	0.42	0.31	--[2]	--[2]	0.38	0.32
	ε_S	2.49	4.71	0.08	0.38	--[2]	--[2]	0.58	0.62
22 May 2016	ε_A	1.96	3.92	1.39	1.61	--[2]	--[2]	2.63	5.01
6:00 – 10:00	ε_D	2.17	3.72	1.12	0.28	--[2]	--[2]	0.16	0.3
	ε_S	2.99	8.28	0.65	0.57	--[2]	--[2]	0.33	0.63
29 June 2016	ε_A	1.19	4.95	1.45	1.08	--[2]	--[2]	3.03	2.97
6:00 – 10:00	ε_D	1.38	4.22	0.5	0.3	--[2]	--[2]	0.18	0.18
	ε_S	2.88	11.23	0.22	0.5	--[2]	--[2]	0.31	0.32
15 August 2016	ε_A	0.84	2.32	0.95	0.77	--[2]	--[2]	3.62	2.71
9:00 – 13:00	ε_D	1.09	1.88	0.1	0.2	--[2]	--[2]	0.22	0.16
	ε_S	0.81	6.04	0.1	0.38	--[2]	--[2]	0.37	0.27
5 September 2016	ε_A	2.57	3.81	2.19	1.64	--[2]	--[2]	5.8	3.68
13:30 – 18:30	ε_D	2.84	3.49	1.07	0.33	--[2]	--[2]	0.34	0.23
	ε_S	4.19	8.25	0.43	0.78	--[2]	--[2]	0.59	0.42

[1] Time series data unavailable
[2] Data is unsuitable for use

Table A.10 Estimated amplitude of ~25 minute period seiche–BSM

Seiche Event Window	*Strain*	*B944*		*B208*		*B206*		*B950*	
		Amp. (ns)	*RMSE*	*Amp. (ns)*	*RMSE*	*Amp. (ns)*	*RMSE*	*Amp. (ns)*	*RMSE*
26 August 2011	ε_A	0.26	4.46	--[2]	--[2]	0.42	1.07	--[1]	--[1]
3:00 – 7:00	ε_D	0.53	4.95	--[2]	--[2]	0.14	0.4	--[1]	--[1]
	ε_S	1.18	6.27	--[2]	--[2]	0.19	0.82	--[1]	--[1]
12 July 2012	ε_A	0.85	7.66	--[2]	--[2]	0.35	1.72	--[1]	--[1]
9:00 – 13:00	ε_D	0.71	6.85	--[2]	--[2]	0.06	0.5	--[1]	--[1]
	ε_S	0.79	16.21	--[2]	--[2]	0.11	1.25	--[1]	--[1]
27 September 2014	ε_A	1.11	4.66	1.02	2.49	--[2]	--[2]	3.2	6.49
10:30 – 14:30	ε_D	0.99	4.71	0.82	0.65	--[2]	--[2]	0.21	0.48
	ε_S	1.63	11.5	0.23	0.88	--[2]	--[2]	0.38	0.83
27 October 2014	ε_A	0.49	4.01	0.36	1.17	--[2]	--[2]	0.73	2.64
8:00 12:00	ε_D	0.28	4.01	0.12	0.32	--[2]	--[2]	0.04	0.13
	ε_S	0.37	7.72	0.17	0.51	--[2]	--[2]	0.09	0.29
2 November 2014	ε_A	1.71	5.04	0.52	2.96	--[2]	--[2]	0.66	6.18
10:00- 14:00	ε_D	1.12	4.17	0.2	1.18	--[2]	--[2]	0.07	0.38
	ε_S	2.37	9.11	0.24	1.1	--[2]	--[2]	0.1	0.67
22 December 2014	ε_A	1.39	3.65	0.59	1.41	--[2]	--[2]	2.81	3.9
8:00 – 12:00	ε_D	1.49	3.03	0.19	0.22	--[2]	--[2]	0.32	0.36
	ε_S	0.22	6.71	0.34	0.54	--[2]	--[2]	0.31	0.41
15 March 2015	ε_A	1.17	3.34	0.47	1.54	--[2]	--[2]	1.17	5.42
13:00 – 17:00	ε_D	1.38	3.47	0.18	0.57	--[2]	--[2]	0.08	0.41
	ε_S	0.46	7.84	0.11	0.6	--[2]	--[2]	0.12	0.55
5 August 2015	ε_A	2	2.88	2.21	1.62	--[2]	--[2]	1.99	3.54
8:00 – 12:00	ε_D	2.11	2.82	0.41	0.38	--[2]	--[2]	0.13	0.28
	ε_S	0.94	5.71	0.44	0.49	--[2]	--[2]	0.24	0.39
31 October 2015	ε_A	0.92	3.08	0.22	1.79	--[2]	--[2]	1.14	5.6
8:00 – 12:00	ε_D	1.03	3.16	0.45	0.3	--[2]	--[2]	0.03	0.35
	ε_S	0.88	4.74	0.08	0.38	--[2]	--[2]	0.13	0.66
22 May 2016	ε_A	1.43	3.96	0.51	1.65	--[2]	--[2]	2.51	5.06
6:00 – 10:00	ε_D	1.32	3.81	0.16	0.48	--[2]	--[2]	0.15	0.31
	ε_S	0.37	8.31	0.18	0.62	--[2]	--[2]	0.27	0.63
29 June 2016	ε_A	0.48	5.0	0.96	1.19	--[2]	--[2]	0.51	3.22
6:00 – 10:00	ε_D	0.65	4.3	0.61	0.27	--[2]	--[2]	0.03	0.19
	ε_S	0.69	11.41	0.18	0.5	--[2]	--[2]	0.07	0.34
15 August 2016	ε_A	0.72	2.38	0.66	0.82	--[2]	--[2]	0.56	3.06
9:00 – 13:00	ε_D	0.71	1.95	0.26	0.18	--[2]	--[2]	0.03	0.18
	ε_S	0.71	6.04	0.19	0.37	--[2]	--[2]	0.11	0.3
5 September 2016	ε_A	0.17	3.97	1.11	1.77	--[2]	--[2]	1.24	4.14
13:30 – 18:30	ε_D	0.22	3.68	0.65	0.44	--[2]	--[2]	0.07	0.25
	ε_S	0.93	8.44	0.41	0.78	--[2]	--[2]	0.19	0.46

[1] Time series data unavailable
[2] Data is unsuitable for use

VITA

Kevin James Gryger, a native of Delran, New Jersey, received two Bachelors of Science degrees at the Richard Stockton College of New Jersey in 2012. After, he worked for the Geoservices segment of Schlumberger in the Gulf of Mexico out of Louisiana. Wanting to advance his education, he made the decision to enter graduate school in the Department of Geology and Geophysics at Louisiana State University. Kevin will receive his master's degree in May 2017. After graduation Kevin plans to begin working on his doctorate.